~~Uncertainty~~ Sensitivity of ~~Antarctic~~ the Bootstrap sea ice concentration ~~using passive microwave retrievals~~ to surface parameters in the Antarctic marginal ice zone using passive microwave retrievals

Marta Stentella[1,2,3], Ghislain Picard[1], Petra Heil[2,4], Jacqueline Boutin[5], Emmanuel Dinnat[6], and Stuart Corney[2,3]

[1]Institut des Géosciences de l'Environnement (IGE),Université Grenoble Alpes, Grenoble, France
[2]Australian Antarctic Program Partnership (AAPP), Hobart, Australia
[3]Institute for Marine and Antarctic Studies (IMAS), University of Tasmania, Hobart, Australia
[4]British Antarctic Survey (BAS), Cambridge, UK
[5]LOCEAN, Sorbonne Université, CNRS, IRD, MNHN, Laboratoire d'Océanographie et du Climat: Expérimentations et Approches Numériques, LOCEAN/IPSL, 75005 Paris, France
[6]NASA Goddard Space Flight Center, Greenbelt, MD, USA

Correspondence: Marta Stentella (marta.stentella@univ-grenoble-alpes.fr)

Abstract. ~~Antarctic sea ice has experienced an unprecedented decline in the past decade (2016-2025).~~ Changes in sea ice concentration (SIC) and derived sea ice extent have been monitored using microwave radiometers since the late 1970s, providing information about the polar response to ~~global~~ climate change, ~~hence~~ making SIC an invaluable variable for numerical models. ~~However, in the~~ Antarctic sea ice has experienced an unprecedented decline in the past decade (2016-2025). In the highly dynamic Marginal Ice Zone (MIZ), the region in between the pack ice and the open ocean, physical properties undergo intense variability, which may impact the accuracy of the SIC products retrieved from brightness temperature measurements. For the purpose of this study, the MIZ is defined as the area with SIC between 15% and 80%. We simulate the variations of brightness temperature due to changes in the physical parameters describing the sea ice, the snow, and the ocean with the Snow Microwave Radiative Transfer Model (SMRT) and the Passive and Active Reference Microwave to Infrared Ocean model (PARMIO) for a range of prescribed SIC. We then apply the core of the Bootstrap SIC algorithm on the simulated brightness temperatures and compare the retrieved ~~and prescribed~~ SIC with the prescribed true SIC, yielding the SIC ~~error~~retrieval uncertainty. This allows us to assess the impact of changes on the SIC retrieval by means of numerical radiative transfer simulations. ~~Our~~ The work identifies the key parameters leading to high uncertainty in the retrieval~~: in~~ . In the snowpack, the liquid water ~~content and~~ fraction, snow grain size, thickness, and snow–ice interface temperature each cause SIC uncertainties ~~of~~ within the 5~~–~~% range, with some parameters reaching up to 10% ~~in the warm conditions MIZ. In the cold season~~depending on the season. However, the most ~~influential factor is~~ dominant uncertainty in the cold season comes from the presence of thin ice ~~, inducing errors up to 30%. Ocean roughness caused by~~ types like dark nilas and grease, characterised by high salinity or liquid water fraction, which induce uncertainties of up to 70%. This uncertainty is comparable to that caused by slush, which can be found in the MIZ all year round. Ocean surface impacted by the high-wind conditions affects both warm and cold seasons and gives rise

to ~~biases up to 15~~uncertainties of up to 10% on the lower SIC MIZ boundary. However, other ~~snowpack~~ parameters that were expected to modify the SIC results, such as the ~~salinity or temperature~~ temperature and salinity in the snowpack overlying the first-year ice, showed a negligible impact in the tested range. We found that the core of the Bootstrap algorithm is largely robust to the variations in the snowpack ~~, with no parameter introducing errors greater than 10% across the MIZ SIC range~~properties. In contrast, ~~ocean surface roughness due to wind speed and~~ the presence of thin ice ~~in the pixel~~ types and slush and ocean surface affected by high wind speeds in the grid cell are the variables leading to the greatest uncertainties, suggesting they are the primary targets to achieve more accurate SIC retrievals in the MIZ.

1 Introduction

The Marginal Ice Zone (MIZ) – the region that separates the pack ice from the open ocean – is a highly dynamic environment featuring continuous interaction between the ocean and the atmosphere (Morison and McPhee, 2001; Bennetts et al., 2022; Dumont, 2022; Vichi, 2022). These exchanges have ongoing impact on the physical structure of the sea ice and the characteristics of the snowpack on top of it (Massom et al., 2001). ~~Physical drivers causing shifts in properties such as temperature, moisture content, or salinity within the snow–sea ice system, or wind speed in the atmosphere, lead to variations in the emissivity of the sea ice, atmosphere and ocean components (Macelloni et al., 2001; Meissner and Wentz, 2002; Mathew et al., 2009; Willmes et al., 2014)). Understanding of~~ Understanding the drivers of the interactions between the sea ice, the ocean, and the atmosphere is essential to explain the factors that contribute to the decline of sea ice extent, including the unprecedented minimum recorded in the Southern Ocean in summer 2023 (Maksym, 2019; Purich and Doddridge, 2023).

The sea ice concentration (SIC) is the fraction of ~~the ocean surface~~ a known ocean area covered by sea ice ~~in a pixel (Comiso, 2009), that is the spatial footprint of the sensor acquiring the measurement~~(Comiso, 2009; Lavergne et al., 2022) . Satellite observations are exploited to retrieve SIC through the brightness temperature (T_B) measured by microwave radiometers in frequencies ~~commonly used in sea ice analysis, between 19 GHz~~ between 6 GHz and 89 GHz, in the vertical (V) and horizontal (H) polarisation ~~(Cavalieri et al., 1984; Swift et al., 1985; Comiso, 1985)~~ (Cavalieri et al., 1984; Swift et al., 1985; Comiso, 1995). Passive microwave (PM) observations are ~~the basic means of investigation~~ valuable to study snow metamorphisms, changes in the physical properties of sea ice, or the ocean surface because they provide synoptic and continuous observations that are independent on daylight conditions and largely unaffected by cloud coverage, not available otherwise (Parkinson and Cavalieri, 2008; Comiso et al., 2017a, b).

The combination of brightness temperature observations at different frequencies or polarisations constitutes a signature that differs across surface types (Comiso et al., 1997). In the case of sea ice, it is dependent on the physical properties of the ice and snow cover. In ~~Antarctica~~the Antarctic, not only the sea ice changes significantly with time and region, but also the snow on top of it. Snow on sea ice undergoes high variability due to redistribution caused by frequent strong winds, seawater flooding, salinity variations and snow ice formation from sea ice overload, and daily melt-thaw cycles. All these processes largely affect the surface and internal properties of the snow, which in turn leads to wide variations in T_B ~~(Massom et al., 2001; Wang et al., 2024).~~

(Macelloni et al., 2001; Massom et al., 2001; Mathew et al., 2009; Willmes et al., 2014; Wang et al., 2024). In addition, the retreat of sea ice means an increased proportion of the marginal ice zone (Strong and Rigor, 2013) and enhanced wave-ice interaction (Bennetts et al., 2022). There is, therefore, an emerging necessity to have more accurate SIC retrieval at low concentration (Kern et al., 2022) and a better understanding of the passive microwave brightness temperature variability in the MIZ. The risk is, otherwise, to mask wave-ice processes with SIC uncertainties (Nose et al., 2020). Understanding the impact of the varying properties of snow and ice on the retrieved SIC ~~, in a rigorous and quantifiable way,~~ remains a challenge in the Southern Ocean (Vichi, 2022), especially in the MIZ (Worby, 2004), where the increasing contribution of the ocean ~~to the pixel~~ (Meissner and Wentz, 2002) to the grid cell signal (due to low SIC), introduces further T_B ~~signature~~ variations alongside the processes of formation and development of sea ice (Matsumura and Ohshima, 2015; Paul et al., 2021).

This study evaluates ~~errors~~ uncertainties in the SIC retrieval induced by changes in the physical properties of the snow–sea ice–ocean system. Building on previous investigations (Andersen et al., 2006; Tonboe et al., 2011; Willmes et al., 2014; Tonboe et al., 2022), we quantify the non-unique relationship between T_B and sea ice concentration, arising from the different snow and ice characteristics that produce different microwave signatures at the same ice concentration. To understand the drivers of the PM signature~~variability~~, we perform a sensitivity analysis on these properties through a ~~forward-modelling approach. We employ a technique based on the Bootstrap algorithm (Comiso, 1986) to compute the SIC from model outputs of each sensitivity experiment and compare the results against a reference simulation, treated as the true SIC . Thus, we evaluate the uncertainty introduced by each parameter on the retrieved SIC. We constrain the area of interest to the low-concentration MIZ, whose boundaries are considered between 15 and 80% SIC (Vichi, 2022)~~radiative transfer computation by perturbing each physical parameter independently to explicitly quantify the brightness temperature variability across the full SIC range, with particular focus on the marginal ice zone. We use a combination of two state-of-the-art radiative transfer models to simulate the passive microwave observations of the ocean and sea ice components of the MIZ~~. These tools allow the simulation of a mixed pixel; representation of the MIZ configuration during~~ , which are then combined to obtain a mixed grid cell for both the warm and cold seasons. ~~The modelling of the sea ice is performed~~ Sea ice is modelled with the Snow Microwave Radiative Transfer Model (SMRT) (Picard et al., 2018), ~~representing~~ which computes the radiative transfer in a multilayer snowpack, sea ice, underlying ocean and overlying atmosphere. The ocean is modelled with the Passive and Active Reference Microwave to Infrared Ocean (PARMIO) (Dinnat et al., 2023), used to simulate the emissivity of the ocean, overlaid by the atmosphere. By employing SMRT and PARMIO together, to have modularity and flexibility, we perform a sensitivity analysis of the physical properties of the sea ice, ocean and atmospheric components, sampling a broad range of parameters drawn from the literature to represent the circumpolar variability across two seasons. This includes the snowpack parameters of first-year sea ice, as well as atmospheric parameters over the open ocean, including wind speed, and ERA5-informed atmospheric profiles. In addition, we simulate the brightness temperature signatures of ice types characteristic of the MIZ, including dark nilas, grease ice and slush and their mixing with the first-year sea ice.

We then employ a technique based on the Bootstrap algorithm (Comiso, 1986) to compute the SIC for each sensitivity experiment and compare the results against a reference simulation, treated as the true SIC. Thus, we evaluate the uncertainty introduced by each parameter on the retrieved SIC as the variability around a reference. The area of interest is the low-concentration MIZ, whose boundaries are considered between 15 and 80% SIC (Strong and Rigor, 2013), and where the ocean contributes strongly to the mixed-grid cell signal, leading to a signature that differs substantially from that of the consolidated ice pack. Accordingly, we chose to work with the Bootstrap algorithm in frequency mode (BF algorithm) as it performs comparatively better in regions dominated by open water (Andersen et al., 2007; Ivanova et al., 2015).

The paper is structured as follows: Sect. 2 provides the background on passive microwave SIC retrieval. Sections 3.1~~and 3.3~~ , 3.2, 3.3 and 3.4 describe the cryospheric~~and ocean components, respectively,~~ , ocean and atmospheric components, for the mixed ~~pixel~~ grid cell simulation. The observations used to support the forward modelling approach are presented in Sect. 3.5. The model parametrisation is adopted to analyse the variability of the snow-covered sea ice signature in Sect. 3.6 and the algorithm for the sensitivity analysis of the ocean and sea ice parameters on SIC simulations is in Sect. 3.7. Results are presented in Sect. 4, first addressing the simulated observational variability (Sect. 4.1) and then the SIC sensitivity analysis (Sect. 4.2). Finally, Sect. 5 discusses the findings, their limitations, and future perspectives.

2 Background

~~Numerous~~ Many SIC retrieval algorithms rely on the contrast of microwave emission between the sea ice (high emission) and ocean (low emission) ~~(Comiso et al., 1984; Steffen and Schweiger, 1991; Comiso, 1985; Markus and Cavalieri, 2000)~~ (Comiso et al., 1984; Steffen and Schweiger, 1991; Comiso, 1995; Markus and Cavalieri, 2000). They assume linear mixing, which means that the T_B observed over a mixed ~~pixel~~ grid cell is the sum of the ~~T_B~~ brightness temperature over its ocean and sea ice components weighted by their respective proportions (Comiso and Sullivan, 1986; Comiso, 2012; Ivanova et al., 2015; Comiso et al., 2017b; Meier and Stewart, 2020). These methods usually evaluate the linear relationship in a two-dimensional space defined by two microwave channels, a channel being the T_B at a given frequency and polarisation, hereafter denoted by its frequency in GHz followed by its polarisation (e.g., 19V). The most commonly used in sea ice studies are the 37V–37H or the 19V–37V, with the latter combination preferred in the Antarctic MIZ, and used in the BF algorithm (Comiso and Sullivan, 1986; Ivanova et al., 2015; Meier and Stewart, 2020).

~~The Bootstrap~~ The BF algorithm (Comiso, 1986) exploits the ~~fact that T_B for an observation P is the linear combination of the pure ocean T_B and pure sea ice T_B to compute SIC:~~ following relation:

$$T_B(P) = T_{\cancel{I}SI}C_I + T_{\cancel{O}OO}(1 - C_I) \quad (1)$$

where C_I is the sea ice concentration, T_B is the observed brightness temperature, ~~T_I is the brightness temperature of sea ice, and T_O is the brightness temperature of the ocean (Swift et al., 1985; Comiso, 1985).~~

~~The observed T_B over pixels with~~ T_{SI} and T_{OO} are the brightness temperatures of 100% ~~ocean~~ sea ice and 100% ~~sea ice tend to appear as two very distinct clusters when represented in~~ ocean respectively, which in the 19V–37V channel space ~~(Swift et al., 1985; Comiso, 1985). The representative brightness temperature of the pure ice and ocean clusters define the tie points T_I and T_O in Eq. 1, respectively, for sea ice and ocean~~tend to appear in two different clusters (Swift et al., 1985; Comiso, 1995), and define the algorithm tie points. Through the sea ice tie point (~~T_I~~T_{SI}), passes a line with a slope determined by ~~daily~~ linear regression of the 100% SIC cluster. Variations along this line result from modifications of sea ice and snowpack properties. Data points distributed around the ocean tie points represent 100% open water with different surface states. The Bootstrap algorithm, among others, adjusts the tie points and the 100% SIC line ~~are adjusted daily~~ on a daily basis to account for the variability that depends on season and ~~the~~ meteorological conditions (Comiso, 2013). The T_B signatures in between these tie points belong to ~~pixels~~ grid cells with different SIC values (Eq. 1). However, different snow and ice characteristics lead to different ~~T_B~~ microwave signatures also when considered in the same concentration, introducing a non-unique relationship between T_B and SIC.

The SIC retrievals are sensitive to variability in the atmosphere and surface emissivity, with the degree of sensitivity depending on the channels employed by the algorithm. One definition of the total uncertainty on SIC retrievals is through two components: the algorithm uncertainty, which includes sensor noise and the residual geophysical variability of the ocean, sea ice and atmosphere, which is the focus of this study, and the smearing uncertainty, arising from the mismatch between satellite footprints and the target grid (Tonboe et al., 2016; Lavergne et al., 2019), which we do not address in this work. Among the algorithm uncertainty components, a first source arises from the surface. The assumption that different ice types lead to distinct brightness temperatures means that ice differing in snow depth, snowpack layering, snow wetness, salinity and temperature yields retrieved SIC values scattered around the true SIC (Tonboe et al., 2011; Willmes et al., 2014; Tonboe et al., 2022). This physical variability of the surface introduces a retrieval scatter even under fully consolidated ice conditions (Kern et al., 2019) , leading unavoidably to uncertainty in the retrieved SIC. A mixture of ice types leads to a non-straight 100% SIC ice line, which, if accounted for, can yield reduced SIC variability (Lavergne et al., 2019; Tonboe et al., 2022), especially when using the BF algorithm. In the Antarctic, surface signature scatter is more pronounced compared to the Arctic, due to snow metamorphism following daily thaw-freeze cycles (Willmes et al., 2014; Kern et al., 2022) and sea ice flooding leading to wet snow ice formation at the interface between the sea ice and the snowpack. In the cold season, the formation of young nilas and grey-white thin ice (< 0.2m) (Ivanova et al., 2015) is characterised by a TB signature intermediate between open ocean and consolidated sea ice, which evolves very rapidly, particularly in the first few hours following formation due to rapid changes in temperature and thickness and brine volume drainage (Kwok et al., 2007; Naoki et al., 2008). This leads to SIC underestimation across all algorithms (Tonboe et al., 2022) and can affect extended surface areas across multiple grid cells, or sub-grid scale at the opening of leads, producing different signatures even between two consecutive satellite passages. A second source of uncertainty arises from atmospheric variability, mostly over the open ocean. Weather effects, including wind speed, cloud liquid water and water vapour, cause the ocean brightness temperatures to scatter around the open water tie point, introducing random noise in the retrieval (Lavergne et al., 2019), with larger impact at lower SIC compared to fully consolidated ice (Andersen et al., 2006; Lavergne et al., 2019; Kern et al., 2019). This noise can be partially reduced through numerical weather predictions, radiative transfer models applied regionally (Andersen et al., 2006; Kern, 2004), weather filters (Cavalieri et al., 1995) and atmospheric correction. However, these corrections have limitations: when atmospheric conditions are moderate and cloud liquid water or water vapour content is low, weather filters can erroneously suppress the sea ice signal, setting SIC to 0% particularly near the ice edge (Andersen et al., 2006; Spreen et al., 2008; Lavergne et al., 2019) . These sources of uncertainty manifest differently depending on concentration, regime and season. The variability increases from winter to early summer (Willmes et al., 2014). In early summer, most SIC products show overestimation at higher concentrations and underestimation in the marginal ice zone (Kern et al., 2019). Generally, most products tend to underestimate SIC when concentrations are below 50% (Kern et al., 2019). Such over- and underestimation (Ivanova et al., 2014) introduces errors in informing climate models (Niederdrenk and Notz, 2018), motivating continued efforts in algorithm development, intercomparison (Ivanova et al., 2015) and validation against both in-situ and satellite observations (Andersen et al., 2007; Tonboe et al., 2016; Kern et al., 2019; Lavergne et al., 2019; Kern et al., 2022), including the capability to transition consistently between the summer and winter seasons. The underestimation is particularly pronounced in the MIZ, where the presence of thin and mixed ice types makes SIC retrieval especially challenging.

3 Methods and Data

3.1 Cryospheric brightness temperature simulation

3.1.1 ~~Snow and thick first-year sea ice simulation~~

We employ the SMRT model (Picard et al., 2018) to simulate the snow-covered sea ice ~~system~~and the thin ice systems. The output ~~is the~~ of this 1D model is the observed T_B at the 19V and 37V channels for a ~~pixel~~ grid cell fully covered by sea ice. The input to the model describes the medium, a stack of horizontal layers and the selected theoretical framework to compute the electromagnetic interaction within the layers. Here, the calculation of the scattering and absorption coefficients is performed using the symmetrized strong contrast expansion (SymSCE) theory (Torquato and Kim, 2021; Picard et al., 2022b) that features a continuous scattering coefficient across the full density range, also at intermediate densities around $468\,\mathrm{Kgm^{-3}}$ (Picard et al., 2022b). The radiative transfer equation is then solved with the discrete ordinate and eigenvalue method (DORT), with 128 streams. The permittivity model for any ice–saline water mixture is obtained by mixing the ice permittivity computed through the Matzler formula (Mätzler, 2006), with the saline water permittivity at each frequency, computed through the formulation by Meissner and Wentz (Meissner and Wentz, 2004), using the Polder van Santen (pvs) mixing formula (Polder and Van Santeen, 1946). The liquid water fraction (LWF) is defined here as the volumetric fraction of liquid water within the considered ice layer, i.e. the ratio between the volume of liquid water and the total volume of the layer. Values therefore range between 0 and 1 and are dimensionless. In all the sea ice layers, modelled with the `make_ice_column` function in SMRT, the microstructure model is described with the hard spheres without stickiness (Tsang et al., 1985; Macelloni et al., 2001; Picard et al., 2014) where the sphere radius in Tables 1 and 2 is the size of the scatterer in the sea ice type considered. In addition, no roughness length scale is taken into account for any sea ice type. In the sea ice simulations, the boundary condition for the radiative transfer equation is imposed by activating the "water substrate" for the lowest layer in SMRT, which represents the ocean beneath the ice. Finally, the sensor employed in the simulations is AMSR2, using the $19\,\mathrm{GHz}$ and $37\,\mathrm{GHz}$ channels, both with an incidence angle of $55\,°$.

We investigate four sea ice surface types that can be found in the MIZ: snow-covered first-year ice, representing the 100% SIC tie point, with simulations capturing the circumpolar variety of first-year ice and snow characteristics; thin ice, dark nilas in the WMO nomenclature (Comiso, 2010), newly formed ice up to $0.05\,\mathrm{m}$ thick with no snow cover; slush represented as a snowpack saturated with ocean saline water, which arises from processes of wave-ice interactions or intense snowfall events over the open ocean surface; and grease ice, modelled as the first accumulation of frazil columnar ice at the ocean surface.

3.1.1 Snow and thick first-year sea ice simulation

We selected the snowpack layering over the first-year sea ice at 100%, based on the frequency of occurrence of the layers in Massom et al. (2001). The final configuration consists of a top one-layer ~~atmospheric layer~~atmosphere, a surface windpacked layer (SP), an underlying depth hoar layer (DH), a snow ice layer (SI) at the snow–ice interface and two superimposed sea ice layers ~~. The windpack~~ (SI_1, SI_2). The windpacked here refers to a wind slab characterised by small grain size~~, while the~~. The depth hoar, usually forming during the cold season due to the temperature gradient in the snowpack~~deriving from the difference between that of~~, derives from the temperature difference between the sea ice underneath and ~~that of~~ the atmosphere (Akitaya, 1974) ~~,~~ and is characterised by larger grains. ~~To describe the low-concentration MIZ, we include~~ On the sea ice surface, we impose a snow ice layer forming through flooding by ocean water during intense snowfall events and characterised by large grain sizes, elevated salinity, and higher density relative to the overlying snow layers (Massom et al., 2001). The first-year ~~sea ice~~ ice is represented by two layers: a thinner, colder upper layer ~~representative of the transitional conditions between the snowpack and the ice,~~ and a thicker lower layer in contact with the ocean, which is slightly less saline.

The overlying layer is a simple bulk atmosphere (`simple_atmosphere` in SMRT) where we prescribe angle-dependent emission in the upward (atmosphere to sensor) and downward (atmosphere to Earth to sensor) directions for each frequency channel, as well as an input value for the atmospheric transmittance. These parameters are taken from the PARMIO output look-up tables and are thus consistent with those used in the ocean simulations to ensure coherence between the modelled sea ice and ocean systems.

The snow layers are modelled with the `make_snowpack` function in SMRT. The microstructure model used for the snow layers is the ~~`unified_scaled_exponential` (Picard et al., 2022a)~~unified scaled exponential (Picard et al., 2022a), which takes the microwave grain size l_{MW} as input (Picard et al., 2022a). We compute l_{MW} as the product of the polydispersity and the Porod length. The microwave polydispersity value (Picard et al., 2022a) is set to `0.7` for the ~~windpack~~ windpacked and `1.5` for the depth hoar and the snow ice. The Porod length is computed as:

$$l_p = \frac{4(1-\rho_{\text{snow}}/\rho_{\text{ice}})}{\text{SSA}\cdot\rho_{\text{ice}}} \quad (2)$$

where the SSA (the specific surface area of snow) is ~~obtained from~~ defined as SSA $= \frac{3}{r\cdot\rho_{ice}}$, obtained from r, the snow optical radius referred to as snow grain size in Table 1 ~~. The ice permittivity model is obtained by mixing the saline water permittivity at each frequency through the formulation by Meissner and Wentz (Meissner and Wentz, 2004), and the pure ice permittivity through the Matzler formula (Mätzler, 2006), using the Polder van Santen (pvs) formula (Polder and Van Santeen, 1946)~~and hereafter, and ρ_{ice} the ice density.

Both layers of sea ice use the type "first-year ice" defined in SMRT. ~~Their thicknesses are of the order of 5 cm and~~ The thick sea ice layer in contact with the ocean is characterised by a vertical temperature gradient characteristic of first-year ice (Lewis et al., 2011), described by linear interpolation between the sea ice layer on the top (SI_1~~m~~

~~for the thin and thick layer, respectively. The microstructure model is described with the hard spheres without stickiness (Tsang et al., 1985; Macelloni et al., 2001; Picard et al., 2014)~~) and the temperature of the ice in contact with the ocean (271 K in Table 1).

The ~~calculation of the scattering and absorption coefficients is performed using the improved Born approximation (IBA)~~snowpack layer ordering follows the sequence listed in Table 1.

3.2 Dark nilas, slush, and grease simulation

Dark nilas is represented in SMRT as a stack of three layers with physical characteristics described in Table 2 where the fixed bulk salinity corresponds to the mid-range value for newly formed ice of this thickness (Weeks and Lee, 1962; Kovacs, 1996). A vertical temperature gradient is prescribed across the layers (Table 2), where the intermediate layer temperature is interpolated linearly between the two boundary values. The brine volume fraction is fixed, across all three layers, at 0.2 (value computed at 269 K, representative of near-freezing temperatures characteristic of ice in the first hours after formation, following Leppäranta and Manninen (1988)). ~~The radiative transfer equation is then solved with the discrete ordinate and eigenvalue method (DORT), with 128 streams~~

Slush is modelled using the newly introduced `make_slush` function in SMRT, which generates a saturated layer composed of a mixture of saline water and ice with no air inclusions.

3.2.1 ~~Thin ice simulation~~

~~Thin ice is modelled as a single layer of type "first-year sea ice" and the two main parameters are the thickness of 0.05 and the salinity of 13~~Grease ice is represented as a thin slush layer consisting of saline water, and frazil ice crystals described with an elongated needle geometry (Comiso, 2010). This geometry influences the absorption coefficient but not the scattering. The water temperature is held constant at 271.25 ~~. The microstructure is modelled with the sticky hard sphere as in the thick sea ice simulations~~ K (Paul et al., 2021). Coherently with the other simulations we use DORT, but for the thin layer of grease, we enabled the coherent layer processing (Mätzler and Wiesmann, 2012; Montpetit et al., 2013).

3.3 Ocean brightness temperature simulation

We use PARMIO model (Dinnat et al., 2023), to simulate the ocean T_B at 19 GHz and 37 GHz. PARMIO models the emissivity of a flat ocean using Fresnel coefficients driven by the seawater permittivity model from ~~Meissner and Wentz (Meissner and Wentz, 2004)~~Meissner and Wentz (2004). Ocean surface waves represented through ~~the Durden-Vesecky wave spectrum (Durden and Vesecky, 1985)~~ Elfouhaily et al. (1997) wave spectrum multiplied by a factor 1.25 contribute to the T_B perturbation and are simulated with a two-scale model. The scattering of small waves, which are less than 4 times the radiometer wavelength, is calculated with the Small Perturbation Method (SPM) while the scattering of the large waves is calculated with the geometrical optics (GO) model. The small waves are taken into account in the Donelan et al. (1993) description for the drag coefficient, while the large waves impact through the Elfouhaily et al. (1997) sea spectrum model. A further contribu-

Table 1. ~~Physical properties of~~ Reference parameter values for the ~~snowpack input~~ summer and winter sea ice profiles used in ~~the SMRT model for warm~~ this study, with their ranges of variability and ~~cold seasons~~literature references. 'Value REF' is the reference value most representative of seasonal observations. The 'Min' and 'Max' columns define the parameter range used in the sensitivity analysis, if they are not provided, the parameter is kept constant.

Parameter	**Summer**			**Winter**			**Reference**
	Value REF	**Min**	**Max**	**Value REF**	**Min**	**Max**	
Winded snowpack							
Thickness (m)	0.1	0	0.2	0.08	0	0.2	(Massom et al., 2001)
Density (kg m^{-3})	370	310	450	300	300	420	(Massom et al., 2001)
Temperature (K)	273	263	273	269	259	273	—
Snow grain size (μm)	50	50	400	100	100	300	—
Salinity (PSU)	1	0	3	1	0	3	(Lewis et al., 2011)
Liquid water fraction (%)	0.5	0	10	0	0	4	(Nicolaus et al., 2009)
Depth hoar							
Thickness (m)	0.01	0	0.1	0.03	0	0.1	(Lewis et al., 2011)
Density (kg m^{-3})	250	200	300	310	200	345	(Massom et al., 2001)
Temperature (K)	273	263	273	270	263	273	—
Snow grain size (μm)	300	50	500	200	200	450	—
Salinity (PSU)	5	0	8	5	0	8	(Massom et al., 2001)
Liquid water fraction (%)	2	1	10	2	0	4	—
Snow ice							
Thickness (m)	0.02	0	0.3	0.1	0	0.4	(Lewis et al., 2011)
Density (kg m^{-3})	600	400	800	500	400	800	(Lewis et al., 2011)
Temperature (K)	272	267	273	271	267	272	(Lewis et al., 2011)
Snow grain size (μm)	400	200	600	400	200	500	—
Salinity (PSU)	5	3	30	5	3	24	(Massom et al., 2001; Jutras et al., 2016)
Liquid water fraction (%)	3.5	0.1	40	2.5	0.1	40	(Jutras et al., 2016)
Sea ice 1							
Thickness (m)	0.05	0	0.1	0.05	0	0.1	—
Density (kg m^{-3})	915	–	–	915	–	–	—
Temperature (K)	269	255	272	268	244	272	(Massom et al., 2001)
Sphere radius (μm)	2	–	–	2	–	–	—
Salinity (PSU)	8	6	11	8	6	11	(Jutras et al., 2016)
Sea ice 2							
Thickness (m)	0.95	–	–	0.95	–	–	—
Density (kg m^{-3})	915	–	–	915	–	–	—
Temperature (K)	271	–	–	271	–	–	—
Sphere radius (μm)	2	–	–	2	–	–	—
Salinity (PSU)	3	–	–	3	–	–	(Jutras et al., 2016)

tion comes from the foam-covered layer where the foam fraction follows ~~the Monahan description (Monahan and Lu, 1990)~~ Monahan and Lu (1990) and the foam emissivity, the Yin formulation ~~(Yin et al., 2016)~~Yin et al. (2016). The foam fraction varies as a function of ~~the~~ wind speed. The ~~reference ocean~~ output incorporates both the foam impact and the atmospheric contribution as included in the PARMIO model, for the ~~benchmark case~~ ocean reference we choose a wind speed of $15\,\mathrm{ms}^{-1}$. The warm and cold season reference configurations differ ~~for the sea water temperature : 0~~in the sea surface temperature (SST): 273 ~~and -1.9~~K and 271 K respectively.

3.4 Atmosphere brightness temperature simulation

This work employs two different atmospheric models for different analysis. We use the PARMIO model to simulate a clear-sky atmosphere. PARMIO relies on an analytical atmospheric formulation that works worldwide, with the SST as the only input parameter and with constant relative humidity, which is used to compute absolute humidity and water vapour content at each atmospheric layer. The absorption is calculated layer by layer according to the model's built-in vertical profile. This configuration does not include any varying humidity field or additional atmospheric variability. The second atmosphere we employ is simulated with the PyRTLib package (Larosa et al., 2024) embedded in SMRT, which enables the simulation of observations, under a non-scattering Rayleigh approximation for the selected radiometer. The atmospheric vertical profile is from the ERA5 reanalysis (Hersbach et al., 2020) including pressure, air temperature, water vapour (specific and relative humidity), cloud liquid and ice water and ozone of the given date, latitude and longitude of interest. These data are used to estimate the upwelling and downwelling temperature and the transmission in SMRT by selecting the R20 gas absorption model (Meshkov and De Lucia, 2007; Makarov et al., 2011), which provides recently updated gas absorption characteristics, particularly for water vapour and oxygen.

3.5 AMSR-2 passive microwave observations

Advanced Microwave Scanning Radiometer2 (AMSR2) data are extracted from the unified collection of AMSR sensors, NSIDC DAAC Advanced Microwave Scanning Radiometer Unified AMSR-U (Meier et al., 2017). AMSR-2, aboard the Japanese satellite Global Change Observation Mission 1^{st}-Water, "SHIZUKU" (GCOM-W1), provided observations from July 2012. These products include observed T_B and estimated SIC for both ascending and descending orbits. The SIC and T_B are provided on a Southern Hemisphere polar stereographic grid (WGS 84 / Antarctic Polar Stereographic, EPSG:3031) at 12.5 km resolution, with a standard parallel at -71°S and central meridian at 0°. We use T_B at 19 GHz and 37 GHz in vertical polarisation in the ascending orbit under an angle of incidence of 55°~~and on a common grid of 12.5×12.5 resolution~~.

We applied a mask to the dataset to select the sea ice area and a limited portion of adjacent open ocean. The mask was created, for each date using the sea ice concentration (SIC > ~~15%)corresponding to the date under analysis for the warm and cold seasons~~0%), and extending it ~~30~~100 km into the ocean with a circular buffer.

3.6 Microwave brightness temperature modelling across the marginal ice zone: variability of sea ice observations

The first part of this work analyses the spread observed in AMSR2 brightness temperature within the 19V–37V space. ~~We simulate a mixed pixel as the~~ The field-of-view brightness temperature is obtained as the area-weighted linear combination of the ~~T_B of the snow covered sea ice, output of the SMRT (Picard et al., 2018) model (~~point-model outputs (SMRT, Sect. 3.1.1 ~~) and the T_B of the ocean, obtained using PARMIO (Dinnat et al., 2023) (Sect. 3.3)~~ and PARMIO, Sect. 3.3), which follows directly from the additivity of radiance. Each T_B derives from different surface types, and the weights are given by the SIC. This mixing of two 1D model outputs assumes that the vertical extent of the medium (in this context, the sea ice freeboard) is negligible compared to its horizontal extent, and that microwave wavelengths are short relative to any three-dimensional structures present. These assumptions imply that lateral and three-dimensional radiative effects, such as those caused by ice deformation or ridging, are not addressed in this work.

~~First, we select individual days of AMSR2 observations within the warm~~ In the first step, we determine the reference tie points: for each season – the warm season (December to February) and the cold season ~~to generate and calibrate the seasonal tie points through forward modelling. These tie points are the optimal representative for T_O and T_I in Eq. 1, for the selected date. The initial selection~~ (June to August) – we select dates at 15-day intervals over the period 2012–2024, yielding 96 dates per season. This multi-date circumpolar background allows us to identify the regions of the T_B space corresponding to 0% and 100% sea-ice concentration from AMSR2 observations.

The initialization of the physical parameters ~~is~~ and their variation range is then informed by literature ~~(Cox and Weeks, 1974; Brucker et al., 2010; Petrich and Eicken, 2017; Soriot et al., 2022; Lawrence et al., 2024). These parameters are subsequently adjusted to match the observations so that the simulated T_B in the 19V and 37V channels visually overlaps with the~~ (Massom et al., 2001; Nicolaus et al., 2009; Lewis et al., 2011; Jutras et al., 2016; Soriot et al., 2022; Lawrence et al., 20 as shown in Table 1. On this basis, we look for the set of parameters whose forward modelled T_B better reproduces the two AMSR2–observed tie points for the two extreme surface conditions (0% and 100% ~~sea ice and ocean clusters of AMSR2 observations. The reference model configuration chosen for the sea ice is described in Table~~ SIC).

The resulting reference simulations define the seasonal circumpolar tie points T_{SI} and T_{OO} in Eq. 1, representative of mean seasonal conditions rather than the precise daily condition: the first-year sea ice simulation (point X_A in Fig. 1), described through the reference values in Table 1 and Sect.~~3.1.1, and for the ocean~~ 3.1.1 and the ocean simulation (point X_{OO} in Fig. 1), described in Sect. 3.3.

In the second step, we iteratively vary each parameter quantitatively across the range ~~defined by the minimum and the maximum values in Table1~~in Table 1, while keeping ~~the~~ all others constant at ~~the~~ their reference value (Table 1). The parameter range is sampled using 21 evenly spaced values, with a uniform increment. Note that the liquid water fraction sensitivity analysis is performed at a fixed temperature of 273 K.

Finally, in the third step, the ~~linear combination of the derived T_O and T_I at 10% interval (Eq. 1), yields mixed pixel simulations~~ sea ice T_B obtained in the second step is combined with T_{OO} through a SIC-weighted linear combination, yielding mixed grid-cell simulations (e.g. points X_P, Fig. 1) that capture the variability observed in the ~~daily~~ seasonal AMSR2 MIZ observations for different ice types.

3.7 Sea ice concentration sensitivity analysis

3.7.1 SIC sensitivity to snow and sea ice parameters

The sensitivity analysis algorithm for each snow and sea ice physical parameter leverages the tie points ~~from the reference model simulation (Sect. 3.1; 3.3)~~ X_A and X_{OO} and the observational point X_P, determined in Sect. 3.6 and is implemented as follows:

1. ~~Use reference tie points calibrated on the 19V–37V observations as in Sect. 3.6: SMRT output for 100% SIC (point A in Fig. 1), parametrised as in Sect. 3.1.1 and PARMIO output for 100% open ocean (point O in Fig. 1), parametrised as in in Sect. 3.3.~~

2. ~~For each parameter variation across its Table 1 range, iteratively run both models and linearly combine the resulting T_B values (Eq. 1) at 15%, 30%, 50%, and 80% SIC to determine the modelled MIZ mixed pixel signature (points P, Fig. 1) for different ice-types as described in Sect. 3.6.~~

3. Determine the slope of the 100% SIC line (~~line A~~ SIC 100% line in Fig. 1). ~~We~~ For this, we use the least-square linear regression in the two-channel space of the 100% SIC T_B cluster values for the analysed ~~date~~season.

4. Determine the intercept with the 100% SIC line (point ~~I~~ X_I in Fig. 1). To do so, we compute the equation for the line through the modelled observation ~~P~~ X_P (third step of Sect. 3.6) and the ocean tie point ~~O~~X_{OO}.

5. Retrieve the SIC ~~corresponding to each modified configuration~~ via geometric interpolation ~~(Comiso, 1985, 2013)~~ (Comiso, 1995, 2013), computing the ratio :

$$\mathrm{SIC} = \frac{|\overline{OP}|}{|\overline{OI}|} = \left(\cancel{\frac{T_P - T_O}{T_I - T_O}} \frac{T_{X_P} - T_{X_{OO}}}{T_{X_I} - T_{X_{OO}}} \right), \tag{3}$$

where points ~~O, P and I~~ X_I and X_P are determined respectively in steps 1,2 and ~~4.~~ X_{OO} in Sect. 3.3.

6. ~~Calculate~~ For each parameter value, calculate the difference between the retrieved and prescribed ~~SIC for each parameter value.~~ true SIC.

3.7.2 SIC sensitivity to thin ice presence

For each surface type, the tie point X_A of snow-covered first-year sea ice is compared to T_B values obtained by replacing a fraction f of the total sea ice with thin ice at representative values (0%, 15%, 30%, 50%, 80%, 100%), with the remaining fraction $(1 - f)$ being first-year ice. The resulting T_B for the observation (X_P) is computed as a linear combination of the contributions from first-year ice, thin ice, and open ocean, weighted by their respective area fractions.

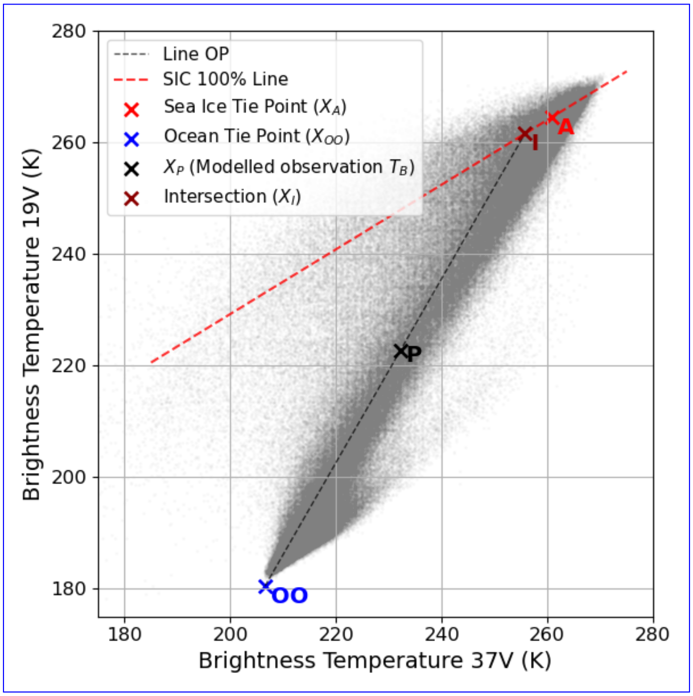

Figure 1. SIC retrieval algorithm description. Brightness temperature at 19V versus 37V from AMSR2 observations (black dots). X_A and X_{OO} are, respectively, the tie points for 100% SIC sea ice (SMRT output for first-year ice) and open ocean (PARMIO output). The top line through tie point X_A (red dashed line) is the linear regression of the 100% SIC cluster. Point X_P is an observational modelled point at true 50% SIC (output of SMRT warm season reference snowpack with dry winded snowpack layer). Line OP (dashed black line) through the ocean tie point and the observation point intercepts SIC 100% line in X_I.

The sensitivity analysis for the thin ~~ice~~ ice–dark nilas component quantifies the impact of different thin ice fractions on ~~total SIC. We compare the T_B of the 100% SIC reference tie point A corresponding to the snow-covered sea ice, computed in section 3.7.1, with the T_B computed when thin ice constitutes a fraction of 0, 0.1, 0.3, 0.5, 0.8 and 1 of the total first-year ice. This analysis is repeated for SIC values of point 2 in Sect. 3.7.1 , and for multiple salinity values across the range specified in Table??. In addition, a range of thicknesses between~~ the total SIC, as a function of temperature profiles, salinity profiles or brine volume fractions in the dark nilas. In the temperature sensitivity experiment for the dark nilas, the top-layer temperature is swept within the range in Table 2 (1 ~~and 7~~K increment), while the bottom layer is held at 271.25 ~~has been tested while holding the reference parametrisation as~~ K and the intermediate layer temperature is interpolated linearly between the two boundary values. The salinity and brine volume fraction are fixed (reference values in Table 2). In the salinity sensitivity experiment, the bulk salinity is varied for the range in Table 2 (1 PSU steps), where the maximum salinity values are recorded as extremes in Tonboe et al. (2026), the brine volume value is computed at 269 K, and all other parameters are kept constant. Finally, for the brine volume fraction sensitivity experiment, the volume fraction ranges from the lower percolation threshold (0.05-0.07, (Cox and Weeks, 1988)) to a maximum of 0.20 for nilas Petrich and Eicken (2017), in 0.005 increments, applied uniformly in the three layers (Table 2).

The sensitivity analysis for the slush component quantifies the impact of different slush fractions on the total SIC, as a function of thickness and liquid water fraction in slush. In the thickness sensitivity experiment, the thickness is sampled at 10 non-uniformly spaced values within the range in Table~~??~~ 2, with finer resolution at smaller thicknesses, while all other parameters are kept constant. In the liquid water fraction sensitivity experiment, the fraction is varied across 14 values in 5% increments within the range in Table 2, while all other parameters are kept constant.

The sensitivity analysis for the grease ice component quantifies the impact of different grease ice fractions on the total SIC, as a function of the liquid water fraction in the grease. The liquid water fraction is varied in 5% increments within the range in Table 2, while all other parameters are kept constant.

3.7.3 SIC sensitivity to wind speed over the ocean~~surface roughness~~

The sensitivity analysis for the ocean component assesses the impact of surface ~~roughness variations~~ T_B variations due to wind speed on SIC. To do so, we ~~use the model setup as described in Sect. 3.3 and we~~ modulate the wind speed in 1 ms^{-1} increments over a range from 2.5 ms^{-1} to 30 ms^{-1}. The SIC sensitivity analysis is analogous to the method described in Sect. 3.7.1 with ~~one modification: in step 2, we vary the ocean physical parameter (i.e., the wind speed) while keeping the reference sea ice tie point A. Each~~ the only modification that the observational point X_P is now represented by each new combination (37V–19V) of ocean T_B resulting from a variation in the wind speed ~~(~~relative to the reference of 15 ms^{-1}~~)~~.

3.7.4 SIC sensitivity to atmosphere variability over ocean

The sensitivity analysis of the atmosphere is conducted by applying varying atmospheric profiles over the ocean surface in SMRT. To sample the atmospheric variability throughout the warm and the cold season, profiles are extracted from ERA5 at a regular spatial grid of longitudes spaced every 60° (6 points) and latitudes at -60°, ~~is considered~~ -65° and -70°S (3 points). Temporally, profiles are sampled every 10 days within the warm season (here define as January–February 2022) and cold season (June–July 2022), yielding 6 dates per month and 108 profiles per season. The surface contribution is taken from the 100% T_B output from the PARMIO model (with the atmosphere deactivated) at wind speed of 15 ms^{-1}, consistently with the ocean simulation described in Sect. 3.3. Each atmosphere object modelled with the *pyrtlib_era5_atmosphere* function in SMRT is overlaid on top of the ocean medium. The resulting T_B, linearly combined with the sea ice tie point (X_A), serve as an observational point ~~P, to which steps 3 to 6 are applied~~ X_P to which the SIC retrieval algorithm is applied (Sect. 3.7.1).

4 Results

4.1 Sensitivity analysis in warm and cold ~~season~~seasons

Table 2. Physical and microstructural properties of thin first-year sea ice (dark nilas), grease ice, and slush used in the SMRT ~~model~~sensitivity analysis. Reference values are used when a parameter is held fixed; Min and Max indicate the range swept when that parameter is varied.

Parameter	**Reference value**	**Min**	**Max**	**Reference**
NILAS				
Total thickness (m)	0.05	–	–	(Petrich and Eicken, 2017)
Layer thicknesses (m)	0.02, 0.02, 0.01	–	–	–
Density (kg m^{-3})	920	–	–	–
Sphere radius (μm)	2	–	–	–
Microstructure model	Sticky hard spheres	–	–	–
Stickiness parameter	100	–	–	–
Top-layer temperature (K)	269.25	260	270.25	(Notz and Worster, 2008)
Middle-layer temperature (K)	270.25	–	–	(Notz and Worster, 2008)
Bottom-layer temperature (K)	271.25	–	–	–
Bulk salinity (PSU)	17	10	45	(Weeks and Lee, 1962; Kovacs, 1996; Tonboe et al., 2026)
Brine volume fraction	0.20	0.05	0.20	(Cox and Weeks, 1988; Petrich and Eicken, 2017)
SLUSH				
Temperature (K)	271.25	–	–	–
Sphere radius (μm)	100	–	–	–
Salinity (PSU)	32	–	–	–
Thickness (m)	0.10	0.01	0.30	–
Liquid water fraction	0.20	0.15	0.80	–
GREASE ICE				
Thickness (m)	0.008	–	–	–
Temperature (K)	271.25	–	–	(Paul et al., 2021)
Sphere radius (μm)	100	–	–	(Paul et al., 2021)
Salinity (PSU)	32	–	–	(Paul et al., 2021)
Inclusion shape	Random needles	–	–	–
Liquid water fraction	–	0.60	0.80	(Paul et al., 2021)

~~During the warm season, the~~ The scatter of the observations around the line connecting the tie points (Fig. 2) is captured through the ~~range of values assumed by the parameters in Table 1~~simulation obtained by varying different physical parameters in their assumed range of values (Table 1). Figure 2 shows that in the warm season, the liquid water ~~content (LWC) exhibits~~ fraction (LWF) and the snow grain size exhibit the greatest variability ~~both~~ in the windpacked layer (Fig. 2~~a) and in the depth hoar (Fig. 2g~~b, c), followed by the thickness (Fig. 2h)~~and the optical radius (Fig. 2e and k)~~. Density, temperature and salinity changes show negligible ~~impact~~ scatter on the T_B across the ~~two snowpack layers~~ snowpack layers SP and DH (Fig. 2~~d, f~~a, d, e, g, h, j and ~~l). On the other hand, thickness , temperature and salinity in the topmost layer of sea ice, show larger changes in~~ k). Despite the slightly wet windpacked (0.5% LWF), thickness and snow grain size changes show noticeable T_B ~~when considering the extremes of the tested range (~~variability, also in the underlying layers (Fig. 2i, l, o, r and u). While variability in T_B due to changes in LWF within the depth hoar layer remains limited, it increases in the snow ice layer, where LWF reaches values typical of saturated snow and slush conditions (Fig. 2n). For the two layers on the bottom (SI and SI_1), the T_B drops significantly when the layer is considered absent in the simulations (null thickness in Fig. 2~~m, n and o~~r and u). The snow–ice interface temperature, represented in the top sea ice layer SI_1 temperature, shows high variability compared to the temperatures in the overlaying layers. The deeper sea ice layer does not affect the ~~T_B~~ microwave signature (result not shown).

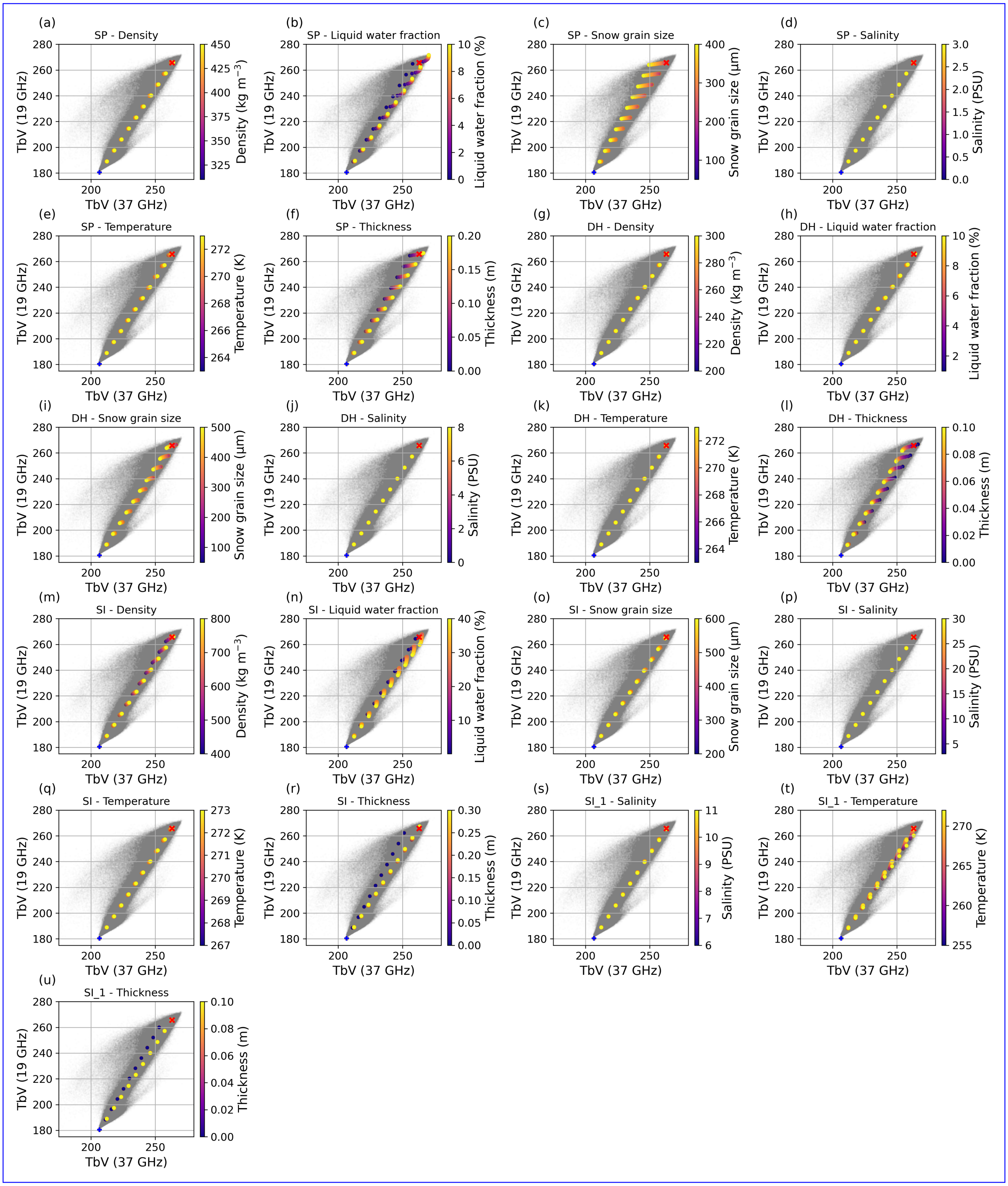

Figure 2. Brightness temperature signature in the 19V–37V space corresponding to variations in the physical properties of sea ice and snowpack layers, as obtained with the three-steps method described in Sect. 3.6. The MIZ T_B observations from AMSR-2 (black dots) represent warm conditions . Each subplot examines a single parameter for a specific layer: windpacked (SP), depth hoar (DH), the snow ice (SI) or top layer of first-year sea ice (SI_1). Data points for 100% SIC (red cross) and open ocean (blue cross) serve as reference tie points. Each data point is coloured by parameter value and it derives from a linear SIC combination (plotted at 10% SIC increments for T_B variability visualization) of modelled variations from the reference configuration.

Figure 3 shows that, in the cold season ~~, parameter changes have~~ characterized by a dry windpacked, the SP top-most layer shows a more contained ~~impact~~ variability in T_B compared to the warm season (Fig. 2~~). This is evident in the snowpack layer (~~b, c and f and Fig. 3~~a to~~ b, c and f). ~~The T_B signature shows highest sensitivity to LWC, optical radius and thickness~~

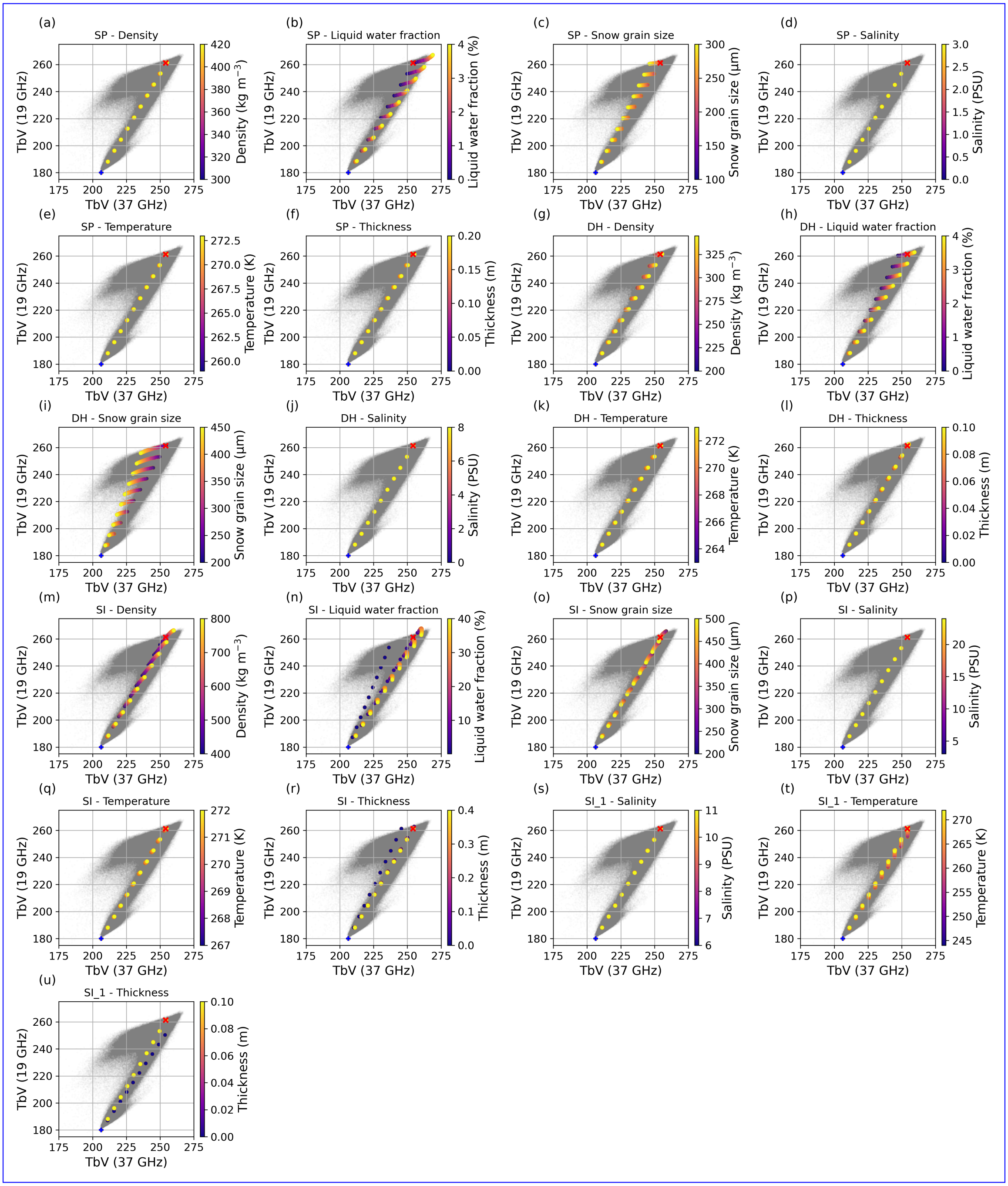

Figure 3. Same as Fig. 2 for cold season conditions.

The brightness temperature shows high sensitivity to LWF and snow grain size; however, unlike the warm condition, this occurs predominantly in the ~~depth hoar layer~~ DH and SI layers (Fig. 3~~g to l)~~ h, i, n and o). Similarly to the warm season, the thickness of the bottom layers (SI and SI_1) shows different T_B when the layer is absent from the simulations (Fig. 3r and u) and the snow–ice interface temperature exhibits high T_B variability.

Figure 4a illustrates the impact of the ~~primary driver of the ocean sensitivity: the wind speed~~wind speed on the microwave signature both with and without the foam contribution. The inclusion of foam makes this parameter a major driver of T_B variability and leads to higher scatter in the simulations. Although wind speeds up to 30 $\mathrm{m\,s^{-1}}$ are considered in the simulations, the spread of the observations is not fully captured by the model chain. However, a significant portion of the observed cluster around the ocean tie point and its trend is reproduced in the output T_{Bs} with foam inclusion at 0% SIC (Fig. 4a).

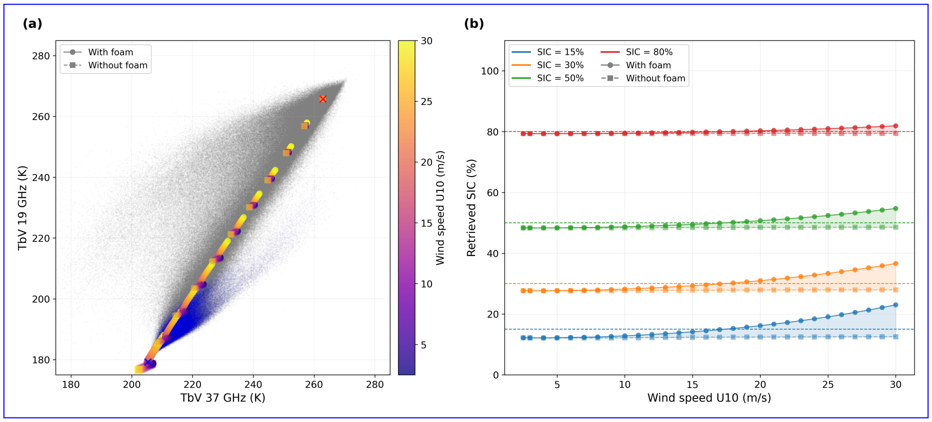

Figure 4. (a) Brightness temperature signature in the 19V–37V space corresponding to wind-induced ocean surface property variations. The MIZ T_B observations (black dots) and open ocean observations (blue dots) from AMSR-2 correspond to warm conditions. Both the observation clusters are masked as described in section 3.5. Each data point is coloured by wind speed value, and it derives from a SIC linear combination (shown at 10% SIC increments). (b) Warm season. SIC retrieved for wind speed variation from the reference ocean parametrisation with foam (15 $\mathrm{m\,s^{-1}}$). True SIC values (15%, 30%, 50%, 80% selected to represent characteristic values across the MIZ range) are shown with horizontal lines. Data points are coloured by SIC and shown for increasing wind speeds from 2 to 30 $\mathrm{m\,s^{-1}}$. The simulations are shown both including the foam effect (circles) or not (squares).

Figure 5 shows that the atmosphere introduces high variability in the open ocean T_B, spreading the T_B across the 0% SIC cluster, primarily with changes in the 37V channel for both seasons.

~~Thin ice~~ Figure 6 shows the scatter of the observations in the 37V-19V plane induced by the presence of dark nilas whose T_B ~~(Fig. 6a)~~ exhibits a wide spread ~~exceeding 20~~reaching 40 K, ~~depending on the salinity~~when the bulk salinity value is at its extreme (Fig. 6a). As shown in Fig. 6a, the thin ice T_B ~~signature~~ is closer to the sea ice tie point at low salinity values. In contrast, at high salinities, characteristic of the initial stages of sea ice growth, the T_B ~~signature~~ shifts towards the ocean ~~reference point~~tie point. Compared to the salinity case, the T_B variability is more limited and closer to the sea ice tie point, but remains significant when the changing parameters are the brine volume fraction (Fig. 6c) and the top-layer temperature (Fig. 6e).

Figure 7 illustrates the T_B changes in the slush simulations when varying the slush layer thickness, which leads to a negligible variation in T_B (Fig. 7a) and in the liquid water fraction which, at its minimum (15%) can yield T_B values higher than the sea

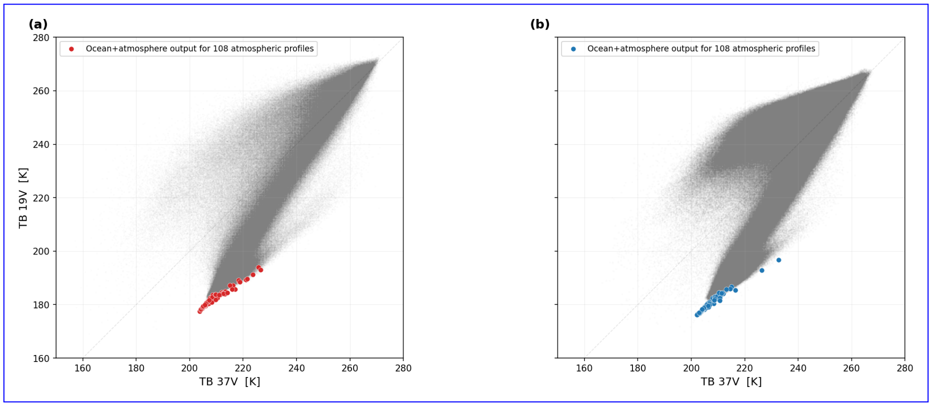

Figure 5. (a) Brightness temperature signatures in the 19V–37V space for 108 atmospheric profiles selected as described in Sect. 3.4 (warm season), superimposed on the open ocean simulation at 15 ms^{-1} wind speed. Sea ice and ocean brightness temperature observations from AMSR2 correspond to the warm season. (b) Same as (a) for the cold season.

ice tie point, while at its maximum (80%) it reaches brightness temperatures close to those of the open ocean. For similarly high LWF values, typical of grease ice, the grease layer exhibits a comparable signature; it ranges from T_B values intermediate between the two tie points to those of the open ocean (Fig. 8a).

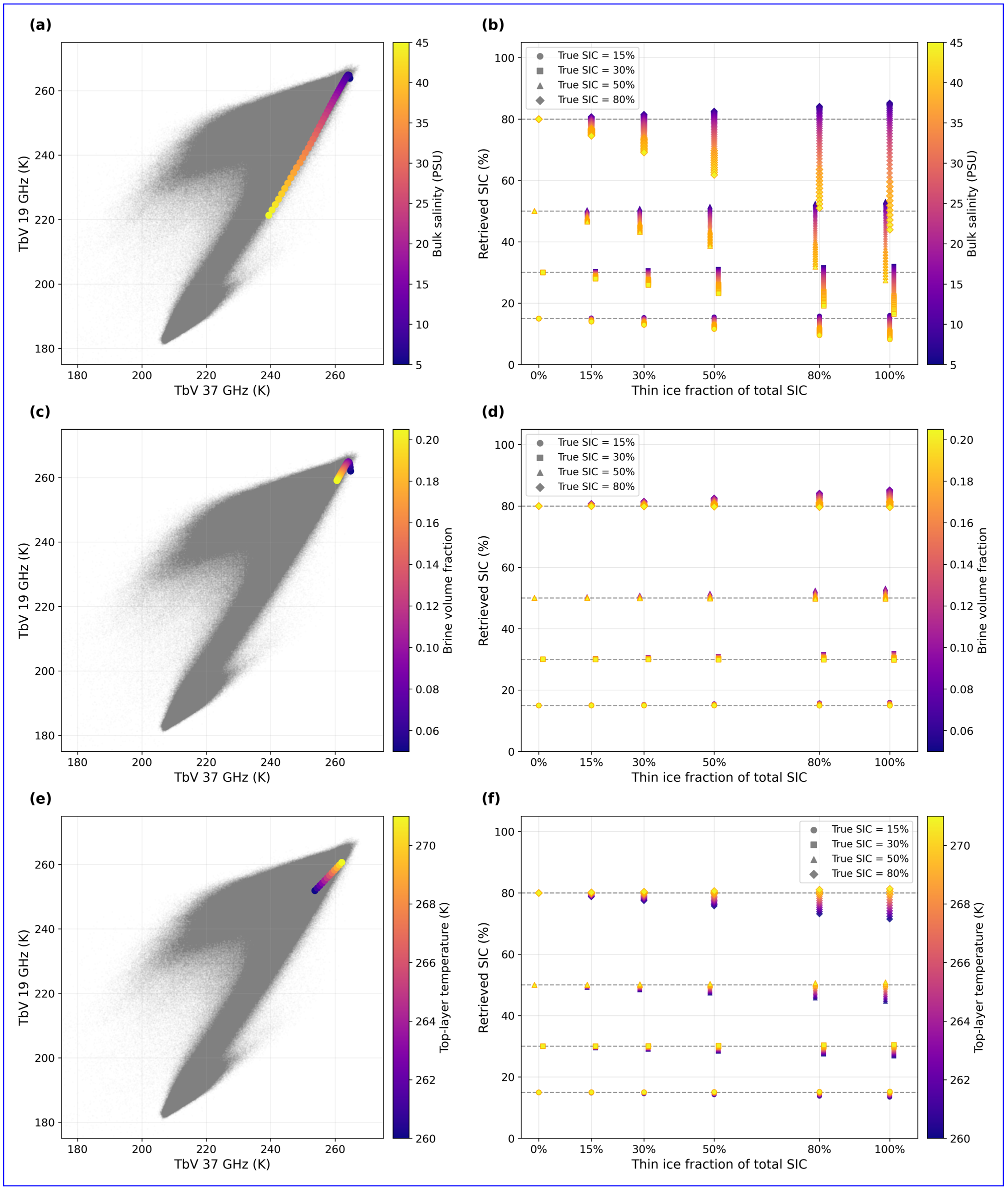

Figure 6. Brightness temperature signature in the 19V–37V space (left column; panels a, c, e) and retrieved SIC (right column; panels b, d, f) for varying proportions of dark nilas mixed with thick first-year sea ice, as obtained with the method described in Sect. 3.5.2. Rows correspond to sensitivity experiments on bulk salinity (a, b), brine volume fraction (c, d), and top-layer temperature (e, f). In the left panels, cold season AMSR-2 observations (grey dots) serve as a background, and each modelled point (100% thin ice cover) is colour-coded by the varied parameter value. In the right panels, the true SIC levels (15%, 30%, 50%, 80%) are marked by horizontal dashed lines, and retrieved SIC values are offset horizontally around each thin ice fraction for visual clarity but computed at the exact fraction values.

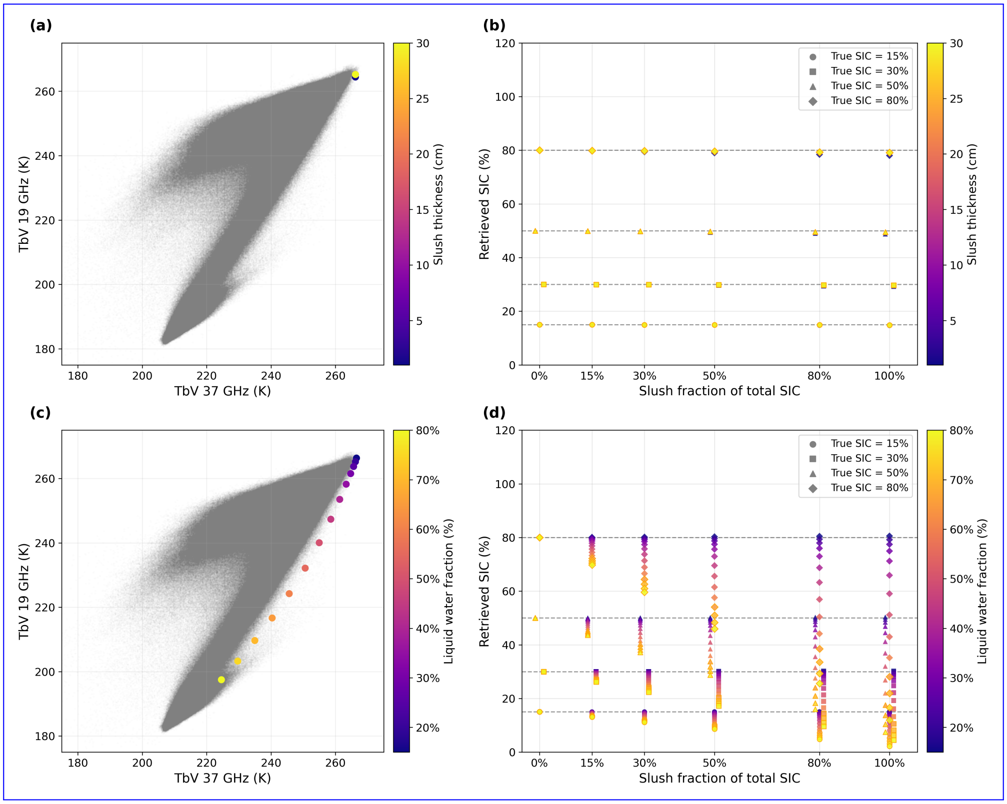

Figure 7. Brightness temperature signature in the 19V–37V space (left column; panels a, c) and retrieved SIC (right column; panels b,d) for varying proportions of slush mixed with thick first-year sea ice. Rows correspond to sensitivity experiments on slush thickness (a, b) and liquid water fraction (c, d). In the left panels, cold season AMSR-2 observations (grey dots) serve as a background and each modelled point (100% slush cover) is colour-coded by the varied parameter value. In the right panels, the true SIC levels (15%, 30%, 50%, 80%) are marked by horizontal dashed lines, and retrieved SIC values are offset horizontally around each thin ice fraction for visual clarity but computed at the exact fraction values.

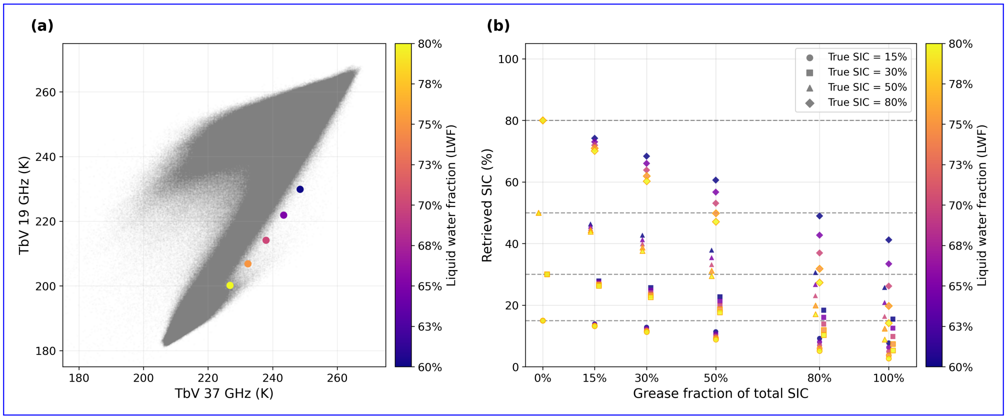

Figure 8. Brightness temperature signature in the 19V–37V space (a) and retrieved SIC (b) for varying proportions of grease ice mixed with thick first-year sea ice. In the left panel, cold season AMSR-2 observations (grey dots) serve as a background and each modelled point (100% grease cover) is colour-coded by LWF value. In the right panel, the true SIC levels (15%, 30%, 50%, 80%) are marked by horizontal dashed lines, and retrieved SIC values are offset horizontally around each thin ice fraction for visual clarity but computed at the exact fraction values.

4.2 Sea ice concentration uncertainty

In line with the sensitivity analysis (Sect. 4.1), the highest impact on the SIC retrieval ~~bias~~ uncertainty (in %), in the warm season, is primarily attributed to the ~~LWC and the optical radius in the snowpack~~ thickness, LWF and the snow grain size in the SP and SI layers (Fig. 9~~d, e), with the windpacked layer being the dominant source of uncertainty (Fig. 9~~a, d and e, blue and purple curves). While for SIC values below 50%, ~~LWC and optical radius induce errors~~ LWF and snow grain size induce uncertainties smaller than 5%; when considering SIC up to 80%, ~~the resulting uncertainty increases, but remains below~~ these uncertainties reach up to 10~~%~~ %. To be noted, the thickness in the snow ice layer induced an uncertainty in the retrieved SIC, mostly when the layer is completely absent (Fig. 9~~d and Fig. 9e).~~ a).

In the depth hoar layer, the thickness, ~~optical radius, and LWC~~ snow grain size, and LWF all contribute similarly, each causing an ~~error within 5% . The thickness and temperature of the uppermost sea ice layer~~ uncertainty within 3% (Fig. 9a, ~~b)impact the simulated SIC at the extremes of their variation range; for instance, when the layer is absent (null thickness).~~ d and e orange curve). All the parameters in the uppermost layer of sea ice show very limited impact on the SIC variability; within 1% and 2%, except for the snow–ice interface temperature, which is a dominating source of uncertainty in SIC. It reaches values as large as 10% over the tested range. (Fig. 9, green lines).

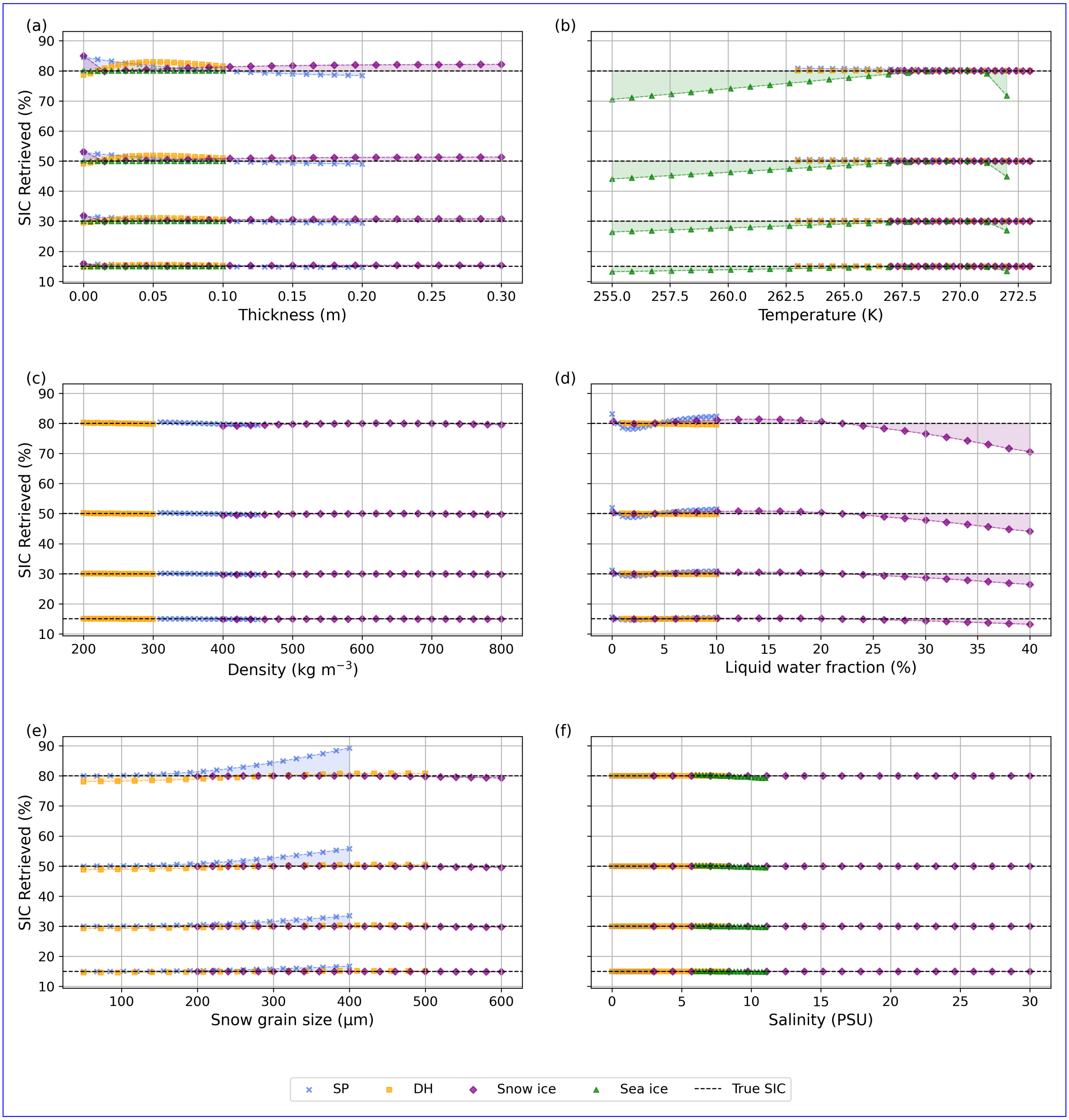

Figure 9. Warm season. SIC retrieved for individual parameter variations from the reference snowpack and sea ice. True SIC values (15%, 30%, 50%, 80% shown to represent characteristic values across the MIZ range) are represented by horizontal lines. For each layer –windpacked (SP, blue crosses), depth hoar (DH, orange squares), snow ice (SI, purple diamond), top first-year sea ice (SI_1, green triangles)– the retrieved SIC is plotted for regularly spaced values within the range defined in Table 1.

Figure ~~??~~ 4b illustrates that SIC retrieval is highly sensitive to changes in ~~ocean surface roughness when the ocean dominates the pixel T_B signature. Towards the lower limit of 15% SIC in the MIZ, errors can exceed~~ the ocean surface at low SIC. When the foam is accounted for in the simulations, the uncertainty can reach values close to 10% under strong wind conditions, up to 30 $\mathrm{m\,s^{-1}}$ whilst at 80% SIC it decreases to 2%. When the foam effect is not included in the simulations, the uncertainty is negligible, indicating the foam is the driver of this uncertainty.

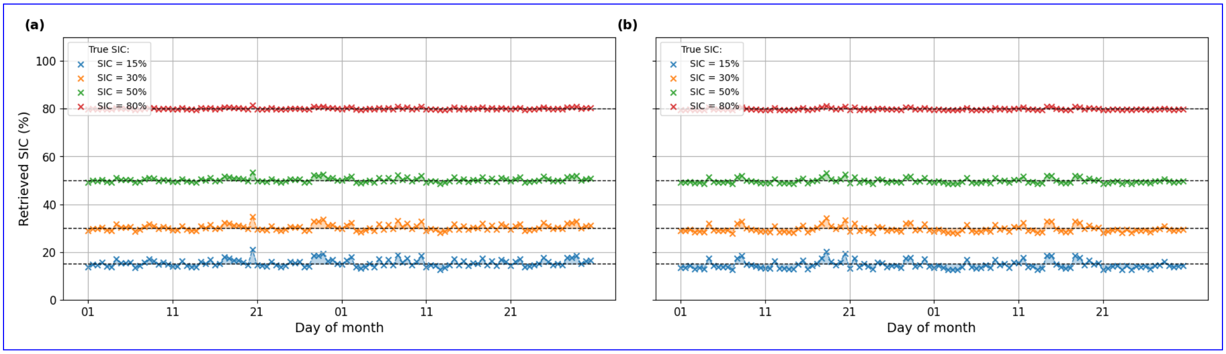

Figure 10. (a) SIC retrieved for different atmospheric profiles selected as in Sect. 3.4 for the warm season. True SIC values (15%, 30%, 50%, 80% shown to represent characteristic values across the MIZ range) are represented with horizontal lines. Data points are coloured by SIC and sampled for the atmosphere at different times and locations, ordered chronologically on the x-axis. (b) Same as (a) for the cold season.

Figure 10a shows that during the warm season, the retrieved SIC under varying atmospheric profiles varies by up to 6% around the 15% true SIC value, whilst at the upper MIZ boundary the variation decreases to 1%.

Figure 11~~d shows that the liquid water content remains the major driver~~ a, d and e show that the thickness, the liquid water fraction and the snow grain size remain the major drivers of the SIC uncertainty in the snowpack layers (SP, DH, SI) in the cold season~~as well. When it exceeds 10% in any snowpack layer~~ , as in the warm season. Compared to the warm season, uncertainties in the dry SP layer are more limited; while when LWF exceeds 5% for wet snow ice, the uncertainty on the higher SIC MIZ boundary (80% ~~) is~~ SIC) is higher but still limited to less than 5% ~~. Slightly wet snow in the top layer leads to SIC underestimation (Fig. 11d blue crosses), but high liquid water content (20%) in the depth hoar (Fig. 11d orange squares), causes overestimation. We observe lower uncertainties affecting the simulated SIC in the cold season compared~~ (compared to 10% in the summer season). Slightly larger is the uncertainty deriving from higher snow grain size in the DH, though this remains well within the 10%.

Similarly to the warm season, the thicknesses of the SI and SI_1 layers yield high SIC uncertainties when the layer thickness is null, reaching a magnitude of more than 10% (Fig. ~~9 versus Fig. 11). All the windpack parameters, for instance, induce negligible errors in the retrieved SIC. Depth hoar thickness and radius have the next most significant influence, yielding uncertainties that remain constrained to less than 5%across the SIC values (Fig. 11a,e)~~11a purple and green line). SIC is insensitive to the thicknesses in the range tested, otherwise. An analogous behaviour between seasons is observed for the snow–ice interface temperature yielding uncertainties up to 10%.

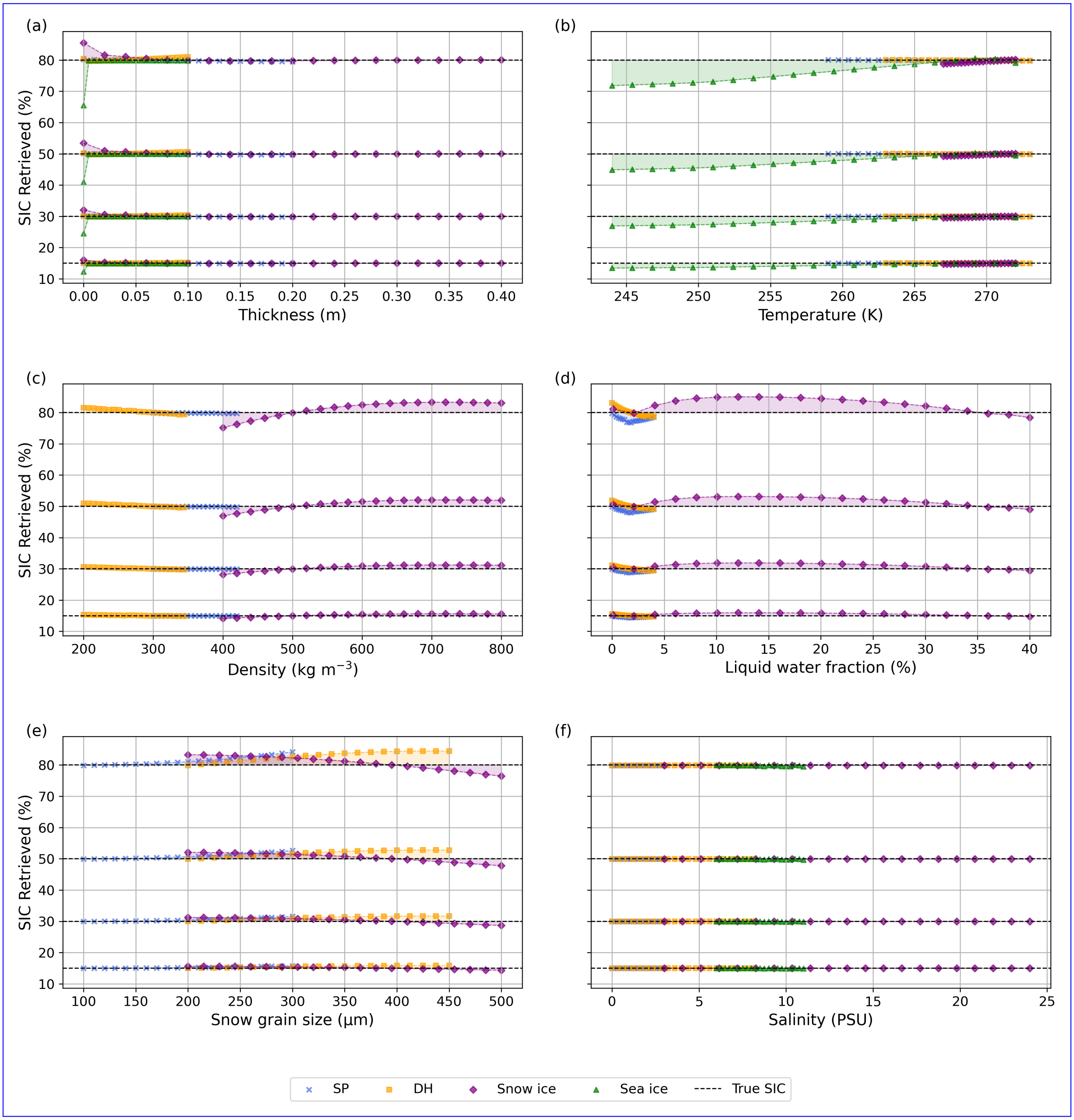

Figure 11. Same as Fig. 9 for cold season conditions. The parameter range is defined in Table 1.

As shown in Sect. 4.1, in the cold season, T_B ~~signature~~ variations in thin ice exceed those of the snowpack ~~, yielding~~ on first-year ice, causing the presence of thin ice to induce substantial ~~biases~~ uncertainties in the retrieved SIC. ~~Inclusion of thin ice with low salinity of approximately 10 PSU~~Figure 6a shows that the inclusion of dark nilas with low bulk salinity values (minimum of 5 PSU) results in a SIC ~~underestimation limited to 10%~~ overestimation limited to 5% when the thin ice occupies the full grid cell at 80% SIC and it is not mixed with first-year ice. However, at ~~higher salinity values and higher thin ice fraction within a pixel~~the maximum tested salinity values (45 PSU), SIC retrieval ~~errors rangebetween 10% and 30~~underestimations can reach 35% (Fig. 6b). In the tested range, the brine volume fraction yields to a maximum overestimation of 5% (Fig. 6d) and the top-layer dark nilas temperature to underestimations within 10% (Fig. 6~~b~~f).

Figures 7b, 7d and 8b show that while slush thickness variations have a negligible impact on the retrieved SIC, the LWF can introduce high uncertainties. This means that when a grid cell at 80% SIC is fully covered by slush, the uncertainty ranges from a small overestimation of less than 1% at low LWF (15%) to an underestimation of nearly 70% at high LWF (80%). Similarly, for grease ice, which is characterised by inherently higher LWF values, the underestimation reaches at least 40 percentage points when the grid cell is fully covered by grease at 80% SIC.

Figure 10b shows that the uncertainties induced from different atmospheric profiles over the ocean in the cold season are comparable to those of the warm season, and limited to 6%, at the lower MIZ boundary (15% SIC).

5 Discussion

In this work, we have considered the variations in physical properties of the ocean surface, the ~~snowpack and the first-year~~ atmosphere, the snowpack and sea ice, to assess their impact on the ~~radiometric signal~~microwave signature. Our analysis identified key variables ~~(e.g., liquid water content, optical radius and thickness~~ to which T_B is more sensitive, namely LWF, snow grain size, thickness and snow–ice interface temperature for the snow-covered sea ice, wind speed for the ocean and ~~highly saline thin ice) to which the T_B signature is more sensitive, leading therefore, to greater errors~~ salinity and LWF for thin ice (Sect. 4.1), which lead to greater uncertainties in the SIC ~~simulated~~ retrieved through the algorithm employed (Sect. 4.2). These simulations allow to reproduce the T_B changes in the 37V–19V space~~, especially in~~. The SIC uncertainties described in this work do not account for the corrections or filters applied to obtain operational SIC products. Rather, it provides an estimate of the T_B variability and the associated SIC uncertainty deriving from the microwave signature of individual surface properties prior to their processing and combination. In line with literature, the ~~warm season (Fig. 2), where the range of parameters, such as the liquid water content or the snow optical radius, shows a broader spread. The snowpack~~ algorithm perform better when the snow is dry, characteristic of the winter season on first-year ice, compared to the summer season, and the highest uncertainties in SIC in the cold season, especially in times characterised by freezing of the ocean surface is to be attributed to thin ice types (Ivanova et al., 2015). Indeed, in the warm season, the snowpack (SP and SI layers) accounts for the greatest variation in the ~~T_B~~ microwave signature, which is therefore reflected in a greater uncertainty in the retrieved SIC. In the cold season, the dry SP layer is largely transparent to microwaves, so variations in T_B in the underlying DH and SI layers become more visible and lead to higher SIC uncertainties than in the warm season, though these remain smaller than the largest uncertainties observed in summer across layers and parameters (Fig. 9; Fig. 11). ~~In line with existing literature, the algorithm provides higher accuracy to snow types in the winter season compared to the summer season(Meier and Notz, 2010; Ivanova et al., 2015). In (Comiso, 2013), the error on the SIC is often limited to 3% during the cold season. On the other hand, during the melt season representedby our modelled warm configuration,~~ An important uncertainty source, independent of the season, is the ~~liquid water content leads to~~

~~a higher imaginary part of the effective permittivity. This means higher absorption and therefore higher emissivity than in dry snow, when considering LWC exceeding 2%-3% (Comiso, 2013). The rise of this value leads to T_B saturation. This process, in~~ temperature at the snow–ice interface, represented, in this study, by the temperature of the top thin layer of ice Fig. 9b, 11b (green curve). This uncertainty, in the upper MIZ limit (80% SIC), reaches about 10 percentage points of underestimation for the lower temperature range tested, results aligned with Tonboe et al. (2022). The underestimation for warmer conditions Fig. 9~~d, introduces uncertainty in the real emissivity of snow and causes an overestimation of SIC~~b, is due to the temperature considered, highly correlated to the brine volume fraction (Leppäranta and Manninen, 1988) when close to the freezing point.

~~During~~ In the cold season, the ~~error~~ uncertainty caused by the cryospheric component is ~~more limited compared to the warm season. This is due to a more constrained T_B variation around the modelled reference snowpack, also noticeable in the observations (Fig. 2 and 3). Deviations from the line through the tie points are therefore limited, resulting in lower biases in the SIC retrieval. On the other hand, the presence of thin ice~~ dominated by the thin ice types: dark nilas, grease and slush. The presence of these ice types produces uncertainties in the simulated SIC, significantly more influential than those from any other parameter ~~in the warm season (Meier et al., 2017)~~(Meier et al., 2017), yielding important SIC underestimations (Cavalieri, 1994; Ivanova et al., 2015). A variation in the ~~thin~~ dark nilas ice fraction included in the first-year sea ice, with salinity values ~~between 15 and~~ around 20 PSU~~can account for errors~~ , for instance, accounts for uncertainties 10-20% larger than those generated by the other snow and sea ice parameters (Fig. 6b). This sensitivity depends on the thin ice development stage ~~, and therefore on its properties , particularly the salinity (Comiso, 2012, 2013), determining~~ (Comiso, 2012, 2013). In this work, the thin ice development is approximated through the variability of the properties of grease ice or the top dark nilas layer, which affects the most the microwave signature at the frequencies used (Naoki et al., 2008). Specifically, the permittivity changes are governed by the LWF for grease ice and by brine for the dark nilas, which in reality vary with increasing ice thickness and age. However, in this work, thickness is varied independently, without being connected to the physical processes that drive changes in the other parameters, for instance through a thermodynamic model. This is reflected in the fact that thickness is not found to be one of the sensitive parameters within the tested range. This is likely due to the low penetration of microwave caused by high salinities and LWF typical of these new ice types, which means reduced ability to obtain true thickness information at these frequencies. As a result, changes in these properties connected to ice age, for instance indirectly through changes in brine volume, are also difficult to detect. By relying solely on the vertical polarization, the BF algorithm is comparatively less sensitive to these properties (Naoki et al., 2008).

Slush in the MIZ can be present year-round and represents a highly wet surface, characterised, in this work as an ice type highly saturated with saline water. This makes it one of the main contributors to the uncertainty near the ice edge, exceeding 20% (Meier and Notz, 2010; Ivanova et al., 2015). This can be seen at high LWF (80%), where the uncertainty reaches 20 percentage points at true SIC 30% and decrease to 10% at 15% SIC.

These properties determine whether the T_B is closer to ~~T_O or T_I~~ T_{OO} or T_{SI}, as observable in Fig. 6~~a~~. As discussed by (Comiso, 1995) in the description of the Bootstrap algorithm in frequency mode, the radiometric signature of new and thin ice formed in the marginal ice zone typically falls below the line connecting the tie points (X_{OO} and X_A), occupying an intermediate region between the open-water and thick-ice signatures as it can be seen in all the thin ice types modelled (Fig. 6, 7, 8). This means that the presence of newly formed thin ice (thickness <0.3 m) yields lower brightness temperatures associated which cause a lower estimate of SIC through any employed SIC retrieval algorithm (Tonboe et al., 2022), and the presence of thin ice disrupts the linear relationship for the SIC, yielding a nonlinear 100% SIC line. In general, the observed variability already present in a single ice type, combined with the fact that a field of view includes multiple ice types (Tonboe, 2010) whose T_B scatter does not follow the SIC isolines, makes the BF algorithm particularly sensitive to the non-linear distribution along the ice line of T_B in these frequency channels (Lavergne et al., 2019; Tonboe et al., 2022).

The impact of ocean surface variations on the retrieved SIC is limited when approaching areas of consolidated ice (SIC >80%) (Fig. ~~??~~4 b). However, when considering the ice edge (15-30%), the ~~error~~ uncertainty in the SIC retrieved can be up to 10%~~-15%~~, which confirms the difficulty in determining the ice edge (spurious positive SIC), and in providing an accurate SIC estimation under rough ocean surface conditions ~~(?Meier and Stroeve, 2008; Comiso, 2013)~~ (Oelke, 1997; Meier and Stroeve, 2008; Comiso, 2013), and therefore increased emissivity (Oelke, 1997). In addition, these results are limited by the reliability of the models, especially at high wind speeds. PARMIO achieves higher accuracy with wind speed up to 15 ms^{-1} where the model has a bias in T_B that corresponds to an underestimation within 5 K with respect to the observations. Nevertheless, Fig. 4 shows consistency between our simulated ocean T_B and the AMSR2 observations. Under clear sky conditions, considering the wind speed effect alone, the inclusion of foam brings this parameter to be among the dominant contributions to the SIC uncertainty in our simulations (Fig. 4). On the other hand, simulations excluding foam show very limited variations even in conditions close to open water, in line with the trend presented in Andersen et al. (2006). This likely reflects the two different consequences of increasing wind speed: the impact, mostly on the H-polarised channel due to the roughness, to which the BF algorithm is insensitive, and the change of permittivity in the surface layer caused by foam air bubbles (relevant from wind speeds over 8 ms^{-1}), which leads to an increase in the V-polarised channel (Kern, 2004), of interest in the BF algorithm.

~~The errors on SIC caused by single parameters are found to agree with those documented in the literature (Ivanova et al., 2015; Comiso, 2009; Andersen et al., 2007). We confirmed larger uncertainties in the warm season, particularly due to increasing open water fractions in the pixel and the presence of liquid water associated with melt in the snowpack (Meier and Notz, 2010). On the other hand, the presence of thin ice is the main contributor to~~ The sensitivity analysis of the atmosphere is conducted over the ocean, where atmospheric effects are more pronounced than over consolidated ice (Andersen et al., 2006). The uncertainty due to the atmosphere is just above 5%, at the lower SIC limit of the MIZ, in agreement with the Oelke (1997) results showing that the combined effect of these of cloud and vapour pressure yield an overestimation of T_B (Andersen et al., 2006) and therefore to uncertainties within 10%, which is usually less than the sum of the independent uncertainties.

As a further point of comparison, the uncertainties provided with the ~~bias in the retrieved SIC , especially in the cold season (Notz and Worster, 2009; Gough et al., 2012)~~NOAA/NSIDC product (Meier et al., 2026) show mean values around 10–15% across 20% to 60% SIC range, with a decrease towards higher SIC in both seasons. Despite the difference between this evaluation and our methodology, the order of magnitude is consistent: near the upper MIZ boundary, the mean is between 5 to 10 percentage points, with more scatter between the year-to-year variability in the warm season. This is in agreement with the uncertainty range derived for each parameter, in the first-year sea ice configuration. The higher uncertainty observed in winter compared to summer in the 20–60% SIC range may be due to the larger impact of higher thin ice fraction, yielding a higher uncertainty in the SIC range.

A first limitation of our ~~modelling approach~~ analysis is that it ~~assumes, as background observations for the forward modelling, a mask including the entirety of~~ treats parameters independently. This conceals potential compensating effects contributing to the SIC uncertainty (Andersen et al., 2006). For example, the ~~circumpolar~~ LWF sensitivity analysis conducted with clear sky atmospheric conditions can have an opposite effect on T_B, yielding smaller SIC uncertainties, however these sensitivity were tested independently. Furthermore, the parameter ranges simulated are broad, meaning that in some cases, the extreme values do not correspond to physically consistent combinations given that they are not constrained to co-vary with one another. Extensions of this work should consider simultaneous variations and their propagation on the SIC retrieval, providing further accuracy to its estimate in the MIZ. This remains, however, a challenge, given the difficulty in identifying and defining the relevant atmosphere–sea ice–ocean interactions to include in thermodynamic models, and the difficulty of measuring them in the field, especially in the MIZ.

A second limitation of our forward modelling approach is that we assume a single observations background across the entire MIZ, thereby not accounting for regional-scale heterogeneity in the snow, ocean, and sea ice~~physical characteristics~~. Future development of this work should focus on a finer scale analysis to capture the ~~physical changes reflected in the parameter range describing the system following intense weather events and ocean forcing. Variations in~~ changes in the physical properties that could otherwise be concealed or averaged, preventing the actual estimation of SIC. ~~In addition, while defining the slope of the 100% SIC line through linear regression as prescribed in the Bootstrap method (Fig. 1) is appropriate at the large scale, it could limit the accuracy of the results on a local scale~~

A remaining challenge concerns the difficulty of modelling the variety of newly formed ice types present in the MIZ, such as pancake ice, for current microwave emission models; therefore, this applies to SMRT.

Another limitation stems from the difficulty of capturing, in the ~~T_B~~ microwave signature interpretation, the strong seasonality of the sea ice characteristics (Comiso et al., 2003). Key processes include snow accumulation and metamorphism leading to intense layering typical of the Antarctic ~~continent~~ sea ice (Massom et al., 2001; Nicolaus et al., 2009; Toyota et al., 2011), surface flooding or~~yet~~, dynamic emissivity profiles for the thin ice depending on its age and thickness (Comiso and Steffen, 2001; Notz and Worster, 2009). Nevertheless, these processes, ~~together with atmospheric effects on T_B~~ exert the largest influence mainly on the polarisation ratio (Cavalieri et al., 1984) which is not used in our method. ~~We relied on 19 and 37 in the vertical channels and a simple one-layer atmosphere.~~

Finally, this ~~analysis treats parameters independently: extensions of this work should consider potential simultaneous variations and their propagation on the SIC retrieval, providing further accuracy to its estimate in the MIZ~~study is restricted to address only a sensitivity analysis of the geophysical noise, represented by the variability of brightness temperatures around the open-ocean and 100% SIC tie points and does not address additional sources of uncertainty related to spatial smearing Lavergne et al. (2019) described in Sect.2.

6 Conclusions

This study ~~set out to differentiate the relevant physical parameters characterising T_B changes that contribute to the variability in passive microwave information of the Southern~~ investigated the sensitivity of passive microwave sea-ice concentration retrieval to a set of environmental parameters, including snow, sea-ice, atmosphere and ocean physical properties, in the Antarctic MIZ, with the aim to ~~infer the impact of different parametrisations on the SIC retrieval~~ better understand the sources of retrieval uncertainty.

~~The response to the specific microwave parametrisation exhibits seasonality.~~ We show that the dominant sources of uncertainty in the warm season are the liquid water ~~content and the optical radius~~ fraction and the snow grain size in the snowpack, for high SIC in the MIZ~~. On the other hand,~~ , while the presence of slush is dominant near the MIZ edge. In this region, another large component in the SIC uncertainty is the ocean surface~~roughness is primarily responsible for biases at low concentrations of sea ice (15% - 30%).~~

~~The cold season shows a similar behaviour in the ocean T_B. However~~, and its combined contribution with that of the atmosphere. The largest effect is due to the high wind speed, leading to the presence of foam in grid cells with a high open ocean fraction.

In the cold season, the T_B ~~signature of the~~ of the dry snow-covered sea ice, undergoes less variation than in the warm season~~, resulting in more accurate SIC retrievals. In contrast, during this season , thin ice (~~; however, all the thin ice types represent the most significant source of uncertainty. More specifically, lower SIC retrieval accuracy in this season is due to the high salinity and liquid water fraction present in the new ice types like grease, dark nilas (thickness < ~~0.1~~0.05 m) or flooded new ice (slush, thickness < 0.3 m)~~represents the most significant source of uncertainty~~.

Our results, derived from the application of a novel forward modelling approach to simulate mixed ~~pixels, identify uncertainties and offer a context for their origin. We~~ grid cells, provide order-of-magnitude quantification of how variations in physical parameter ~~ranges impact SIC inference~~ impact SIC retrievals across different sea ice concentrations in the MIZ. ~~These modelled uncertainties are consistent with literature values derived from applying an operational SIC retrieval algorithm to observations. Importantly, we demonstrated improved sea ice concentration through the interpretation of the radiometric signal using the SMRT and PARMIO models. Applying this method to obtain accurate SIC estimates will deliver enhanced sea ice extent information, especially for regional studies.~~

Code and data availability. The sea ice and ocean configuration files and model outputs generated for this study are available at https://github.com/StentelMarta/Uncertainty_Antarctic_SIC_retrievals.git.

Author contributions. MS and GP designed the analysis method. PH and GP set the context and direction for this study. MS conducted the study and wrote the manuscript. JB and ED participated in the discussion for the parametrisation of the PARMIO model. ED compared the brightness temperatures simulated with the PARMIO model configuration to AMSR2 observations. All co-authors discussed and revised the manuscript.

Competing interests. One of the co-authors, PH, is a member of the editorial board of The Cryosphere.

Acknowledgements. This study is an outcome of the AUFRANDE project, which is co-funded by the European Union under the Marie Skłodowska-Curie Grant Agreement No 101081465 (AUFRANDE). Views and opinions expressed are however, those of the authors only and do not necessarily reflect those of the European Union or the Research Executive Agency. Neither the European Union nor the Research Executive Agency can be held responsible for them. MS and PH acknowledge award #501 of the International Space Science Institute. PH acknowledges support from the Australian Government as part of the Antarctic Science Collaboration Initiative (ASCI000002), and the Australian Government's Australian Antarctic Science Program grant 4625. During the early part of this study, PH was with the Australian Antarctic Division (AAD), Kingston, Australia, as well as on a Fellowship with the Swiss Federal Institute for Snow & Avalanche Research (SLF), Davos, Switzerland.

References

Akitaya, E.: Studies on depth hoar, Contributions from the Institute of Low Temperature Science, 26, 1–67, 1974.

Andersen, S., Tonboe, R., Kern, S., and Schyberg, H.: Improved Retrieval of Sea Ice Total Concentration from Spaceborne Passive Microwave Observations Using Numerical Weather Prediction Model Fields: An Intercomparison of Nine Algorithms, Remote Sensing of Environment, 104, 374–392, https://doi.org/10.1016/j.rse.2006.05.013, 2006.

Andersen, S., Tonboe, R., Kaleschke, L., Heygster, G., and Pedersen, L. T.: Intercomparison of ~~passive microwave sea ice concentration retrievals over the high-concentration~~ Passive Microwave Sea Ice Concentration Retrievals over the High-concentration Arctic~~sea ice~~ Sea Ice, Journal of Geophysical Research: Oceans, 112, 2006JC003 543, https://doi.org/10.1029/2006JC003543, 2007.

Bennetts, L. G., Bitz, C. M., Feltham, D. L., Kohout, A. L., and Meylan, M. H.: Marginal ~~ice zone dynamics: future research perspectives and pathways~~Ice Zone Dynamics: Future Research Perspectives and Pathways, Philosophical Transactions of the Royal Society A: Mathematical, Physical and Engineering Sciences, 380, 20210 267, https://doi.org/10.1098/rsta.2021.0267, ~~number: 2235,~~ 2022.

~~Brucker, L., Picard, G., and Fily, M.: Snow grain-size profiles deduced from microwave snow emissivities in Antarctica~~

Cavalieri, D. J.: A Microwave Technique for Mapping Thin Sea Ice, Journal of ~~Glaciology, 56, 514–526, , number: 197, 2010.~~ Geophysical Research: Oceans, 99, 12 561–12 572, https://doi.org/10.1029/94JC00707, 1994.

Cavalieri, D. J., Gloersen, P., and Campbell, W. J.: Determination of ~~sea ice parameters~~ Sea Ice Parameters with the NIMBUS 7 SMMR, Journal of Geophysical Research: Atmospheres, 89, 5355–5369, https://doi.org/10.1029/JD089iD04p05355, 1984.

~~Comiso, J.: SSM~~

Cavalieri, D. J., St. Germain, K. M., and Swift, C. T.: Reduction of Weather Effects in the Calculation of Sea-Ice Concentration with the DMSP SSM/~~I Concentrations using the Bootstrap Algorithm, NASA RP-1380 (NASA Reference Publication 1380), 1985.~~ I, Journal of Glaciology, 41, 455–464, https://doi.org/10.3189/S0022143000034791, 1995.

Comiso, J.: ~~amsr-atbd-supp12-seaice~~Amsr-Atbd-Supp12-Seaice, 2012, 2012.

Comiso, J., Cavalieri, D., and Markus, T.: Sea ~~ice concentration, ice temperature, and snow depth using~~ Ice Concentration, Ice Temperature, and Snow Depth Using ~~AMSR-E~~AMSR-E~~data~~ Data, IEEE Transactions on Geoscience and Remote Sensing, 41, 243–252, https://doi.org/10.1109/TGRS.2002.808317, 2003.

Comiso, J. C.: Characteristics of Arctic~~winter sea ice from satellite multispectral microwave observations~~ Winter Sea Ice from Satellite Multispectral Microwave Observations, Journal of Geophysical Research: Oceans, 91, 975–994, https://doi.org/10.1029/JC091iC01p00975, 1986.

Comiso, J. C.: ~~Enhanced~~ SSM/I Sea Ice Concentrations ~~and Ice~~Using the ~~Extents~~Bootstrap ~~from AMSR~~Algorithm~~-~~, NASA Reference Publication 1380, 1995.

Comiso, J. C.: Enhanced ~~E~~Sea Ice Concentrations and Ice Extents from AMSR-E Data, https://doi.org/10.11440/rssj.29.199, 2009.

Comiso, J. C.: Polar Oceans from Space, Springer, New York, 1 edn., https://doi.org/10.1007/978-0-387-68300-3, 2010.

Comiso, J. C.: Descriptions of ~~GCOM-W1~~GCOM-W1 AMSR2~~Level~~ Level 1R and Level 2 ~~Algorithms~~Algorithms JAXA, AMSR2 ATBD, 2013.

Comiso, J. C. and Steffen, K.: Studies of Antarctic~~sea ice concentrations from satellite data and their applications~~ Sea Ice Concentrations from Satellite Data and Their Applications, Journal of Geophysical Research: Oceans, 106, 31 361–31 385, https://doi.org/10.1029/2001JC000823, 2001.

Comiso, J. C. and Sullivan, C. W.: Satellite ~~microwave and in situ observations~~ Microwave and in Situ Observations of the ~~Weddell~~Weddell Sea~~ice cover and its marginal ice zone~~ Ice Cover and Its Marginal Ice Zone, Journal of Geophysical Research: Oceans, 91, 9663–9681, https://doi.org/10.1029/JC091iC08p09663, 1986.

Comiso, J. C., Ackley, S. F., and Gordon, A. L.: Antarctic ~~sea ice microwave signatures and their correlation with in situ ice observations~~Sea Ice Microwave Signatures and Their Correlation with in Situ Ice Observations, Journal of Geophysical Research: Oceans, 89, 662–672, https://doi.org/10.1029/JC089iC01p00662, ~~number: C1,~~ 1984.

Comiso, J. C., Cavalieri, D. J., Parkinson, C. L., and Gloersen, P.: Passive ~~microwave algorithms for sea ice concentration~~Microwave Algorithms for Sea Ice Concentration: A~~comparison of two techniques~~ Comparison of Two Techniques, Remote Sensing of Environment, 60, 357–384, https://doi.org/10.1016/S0034-4257(96)00220-9, 1997.

Comiso, J. C., Gersten, R. A., Stock, L. V., Turner, J., Perez, G. J., and Cho, K.: Positive Trend in the ~~AntarcticSeaIce~~ Antarctic Sea Ice Cover and ~~Associated~~Associated Changes in ~~Surface~~Surface Temperature, Journal of Climate, 30, 2251–2267, https://doi.org/10.1175/JCLI-D-16-0408.1, 2017a.

Comiso, J. C., Meier, W. N., and Gersten, R.: Variability and ~~trends~~ Trends in the Arctic~~sea ice cover~~ Sea Ice Cover: Results~~from different techniques~~ from Different Techniques, Journal of Geophysical Research: Oceans, 122, 6883–6900, https://doi.org/10.1002/2017JC012768, 2017b.

Cox, G. F. N. and Weeks, W. F.: ~~Salinity Variationsin Sea Ice~~ Numerical Simulations of the Profile Properties of Undeformed First-year Sea Ice during the Growth Season, Journal of ~~Glaciology, 13, 109–120, , 1974.~~ Geophysical Research: Oceans, 93, 12 449–12 460, https://doi.org/10.1029/JC093iC10p12449, 1988.

Dinnat, E., English, S., Prigent, C., Kilic, L., Anguelova, M., Newman, S., Meissner, T., Boutin, J., Stoffelen, A., Yueh, S., Johnson, B., Weng, F., and Jimenez, C.: PARMIO: ~~AReferenceQuality~~ A Reference Quality Model~~for Ocean~~ for ~~Surface~~Ocean Surface Emissivity and Backscatter from the Microwave to the Infrared, Bulletin of the American Meteorological Society, 104, E742–E748, https://doi.org/10.1175/BAMS-D-23-0023.1, 2023.

Donelan, M. A., Dobson, F. W., Smith, S. D., and Anderson, R. J.: On the Dependence of Sea Surface Roughness on Wave Development, Journal of Physical Oceanography, 23, 2143–2149, https://doi.org/10.1175/1520-0485(1993)023<2143:OTDOSS>2.0.CO;2, 1993.

Dumont, D.: Marginal ~~ice zone dynamics: history, definitions and research perspectives~~Ice Zone Dynamics: History, Definitions and Research Perspectives, Philosophical Transactions of the Royal Society A: Mathematical, Physical and Engineering Sciences, 380, 20210 253, https://doi.org/10.1098/rsta.2021.0253, ~~number: 2235,~~ 2022.

~~Durden, S.and Vesecky, J~~

Elfouhaily, T., Chapron, B., Katsaros, K., and Vandemark, D.: A ~~physical radar cross-section model for a wind-driven sea with swell, IEEE Journal of Oceanic Engineering, 10, 445–451, , 1985.~~ Unified Directional Spectrum for Long and Short Wind-driven Waves, Journal of Geophysical Research: Oceans, 102, 15 781–15 796, https://doi.org/10.1029/97JC00467, 1997.

~~Gough~~

Hersbach, H., Bell, B., Berrisford, P., Hirahara, S., Horányi, A.~~-~~, Muñoz-Sabater, J., ~~Mahoney~~Nicolas, J., Peubey, C., Radu, R., Schepers, D., Simmons, A.~~ R., Langhorne~~, Soci, C., Abdalla, S., Abellan, X., Balsamo, G., Bechtold, P., Biavati, G., Bidlot, J., Bonavita, M., De Chiara, G., Dahlgren, P., Dee, D., Diamantakis, M., Dragani, R., Flemming, J., Forbes, R., Fuentes, M., Geer, A., Haimberger, L., Healy, S., Hogan, R. J., ~~Williams~~Hólm, E., Janisková, M.~~J.~~, Keeley, S., Laloyaux, P., Lopez, P., Lupu, C., Radnoti, G., De Rosnay, P., Rozum, I., Vamborg, F., Villaume, S., and Thépaut, J.-N.: The ERA5 Global Reanalysis, Quarterly Journal of the Royal Meteorological Society, 146, 1999–2049, https://doi.org/10.1002/qj.3803, 2020.

Ivanova, N., Johannessen, O. M., ~~and Haskell, T. G.: Sea ice salinity and structure~~Pedersen, L. T., and Tonboe, R. T.: Retrieval of Arctic Sea Ice Parameters by Satellite Passive Microwave Sensors: ~~A~~A Comparison~~winter time series of salinity and its distribution, Journal of Geophysical Research: Oceans, 117, 2011JC007 527, , 2012.~~ of Eleven Sea Ice Concentration Algorithms, IEEE Transactions on Geoscience and Remote Sensing, 52, 7233–7246, https://doi.org/10.1109/TGRS.2014.2310136, 2014.

Ivanova, N., Pedersen, L. T., Tonboe, R. T., Kern, S., Heygster, G., Lavergne, T., ~~Sørensen~~Sørensen, A., Saldo, R., ~~Dybkjær~~Dybkjær, G., Brucker, L., and Shokr, M.: Satellite ~~passive microwave measurements of sea ice concentration: an optimal algorithm and challenges~~Passive Microwave Measurements of Sea Ice Concentration: An Optimal Algorithm and Challenges, https://doi.org/10.5194/tcd-9-1269-2015, 2015.

Jutras, M., Vancoppenolle, M., Lourenço, A., Vivier, F., Carnat, G., Madec, G., Rousset, C., and Tison, J.-L.: Thermodynamics of Slush and Snow–Ice Formation in the Antarctic Sea-Ice Zone, Deep Sea Research Part II: Topical Studies in Oceanography, 131, 75–83, https://doi.org/10.1016/j.dsr2.2016.03.008, 2016.

Kern, S.: A New Method for Medium-Resolution Sea Ice Analysis Using Weather-Influence Corrected Special Sensor Microwave/Imager 85 GHz Data, International Journal of Remote Sensing, 25, 4555–4582, https://doi.org/10.1080/01431160410001698898, 2004.

Kern, S., Lavergne, T., Notz, D., Pedersen, L. T., Tonboe, R. T., Saldo, R., and Sørensen, A. M.: Satellite Passive Microwave Sea-Ice Concentration Data Set Intercomparison: Closed Ice and Ship-Based Observations, The Cryosphere, 13, 3261–3307, https://doi.org/10.5194/tc-13-3261-2019, 2019.

Kern, S., Lavergne, T., Pedersen, L. T., Tonboe, R. T., Bell, L., Meyer, M., and Zeigermann, L.: Satellite Passive Microwave Sea-Ice Concentration Data Set Intercomparison Using Landsat Data, The Cryosphere, 16, 349–378, https://doi.org/10.5194/tc-16-349-2022, 2022.

Kovacs, A.: Sea Ice Part I. Bulk Salinity Versus Ice Floe Thickness, CRREL Report 96-7, Cold Regions Research and Engineering Laboratory (CRREL), 1996.

Kwok, R., Comiso, J. C., Martin, S., and Drucker, R.: Ross Sea Polynyas: Response of Ice Concentration Retrievals to Large Areas of Thin Ice, Journal of Geophysical Research: Oceans, 112, 2006JC003 967, https://doi.org/10.1029/2006JC003967, 2007.

Larosa, S., Cimini, D., Gallucci, D., Nilo, S. T., and Romano, F.: PyRTlib: An Educational Python-based Library for Non-Scattering Atmospheric Microwave Radiative Transfer Computations, Geoscientific Model Development, 17, 2053–2076, https://doi.org/10.5194/gmd-17-2053-2024, 2024.

Lavergne, T., Sørensen, A. M., Kern, S., Tonboe, R., Notz, D., Aaboe, S., Bell, L., Dybkjær, G., Eastwood, S., Gabarro, C., Heygster, G., Killie, M. A., Brandt Kreiner, M., Lavelle, J., Saldo, R., Sandven, S., and Pedersen, L. T.: Version 2 of the EUMETSAT OSI SAF and ESA CCI Sea-Ice Concentration Climate Data Records, The Cryosphere, 13, 49–78, https://doi.org/10.5194/tc-13-49-2019, 2019.

Lavergne, T., Kern, S., Aaboe, S., Derby, L., Dybkjaer, G., Garric, G., Heil, P., Hendricks, S., Holfort, J., Howell, S., Key, J., Lieser, J. L., Maksym, T., Maslowski, W., Meier, W., Muñoz-Sabater, J., Nicolas, J., Özsoy, B., Rabe, B., Rack, W., Raphael, M., De Rosnay, P., Smolyanitsky, V., Tietsche, S., Ukita, J., Vichi, M., Wagner, P., Willmes, S., and Zhao, X.: A New Structure for the Sea Ice Essential Climate Variables of the Global Climate Observing System, Bulletin of the American Meteorological Society, 103, E1502–E1521, https://doi.org/10.1175/BAMS-D-21-0227.1, 2022.

Lawrence, I. R., Ridout, A. L., Shepherd, A., and Tilling, R.: A Simulation of Snow on ~~AntarcticSeaIce~~ Antarctic Sea Ice Based on ~~Satellite~~Satellite Data and ~~Climate~~Climate Reanalyses, Journal of Geophysical Research: Oceans, 129, e2022JC019 002, https://doi.org/10.1029/2022JC019002, 2024.

Leppäranta, M. and Manninen, T.: The brine and gas content of sea ice with attention to low salinities and high temperatures, https://api.semanticscholar.org/CorpusID:101092290, 1988.

Lewis, M., Tison, J., Weissling, B., Delille, B., Ackley, S., Brabant, F., and Xie, H.: Sea Ice and Snow Cover Characteristics during the Winter–Spring Transition in the Bellingshausen Sea: An Overview of SIMBA 2007, Deep Sea Research Part II: Topical Studies in Oceanography, 58, 1019–1038, https://doi.org/10.1016/j.dsr2.2010.10.027, 2011.

Macelloni, G., Paloscia, S., Pampaloni, P., and Tedesco, M.: Microwave ~~emission from dry snow: a comparison of experimental and model results~~Emission from Dry Snow: A Comparison of Experimental and Model Results, IEEE Transactions on Geoscience and Remote Sensing, 39, 2649–2656, https://doi.org/10.1109/36.974999, 2001.

Makarov, D., Tretyakov, M.Yu., and Rosenkranz, P.: 60-GHz Oxygen Band: Precise Experimental Profiles and Extended Absorption Modeling in a Wide Temperature Range, Journal of Quantitative Spectroscopy and Radiative Transfer, 112, 1420–1428, https://doi.org/10.1016/j.jqsrt.2011.02.018, 2011.

Maksym, T.: Arctic and ~~AntarcticSeaIce~~ Antarctic Sea Ice Change: Contrasts, Commonalities, and Causes, Annual Review of Marine Science, 11, 187–213, https://doi.org/10.1146/annurev-marine-010816-060610, ~~number: 1,~~ 2019.

Markus, T. and Cavalieri, D.: An ~~enhancement~~ Enhancement of the ~~NASA~~NASA Team~~sea ice algorithm~~ Sea Ice Algorithm, IEEE Transactions on Geoscience and Remote Sensing, 38, 1387–1398, https://doi.org/10.1109/36.843033, ~~publisher: Institute of Electrical and Electronics Engineers (IEEE),~~ 2000.

Massom, R. A., Eicken, H., Hass, C., Jeffries, M. O., Drinkwater, M. R., Sturm, M., Worby, A. P., Wu, X., Lytle, V. I., Ushio, S., Morris, K., Reid, P. A., Warren, S. G., and Allison, I.: Snow on Antarctic~~sea ice~~ Sea Ice, Reviews of Geophysics, 39, 413–445, https://doi.org/10.1029/2000RG000085, 2001.

Mathew, N., Heygster, G., and Melsheimer, C.: Surface Emissivity of the ~~ArcticSea~~Arctic Sea Ice~~at AMSR -~~at ~~E~~AMSR-E Frequencies, IEEE Transactions on Geoscience and Remote Sensing, 47, 4115–4124, https://doi.org/10.1109/TGRS.2009.2023667, 2009.

Matsumura, Y. and Ohshima, K. I.: Lagrangian ~~modelling of frazil ice in the ocean~~Modelling of Frazil Ice in the Ocean, Annals of Glaciology, 56, 373–382, https://doi.org/10.3189/2015aog69a657, ~~publisher: International Glaciological Society,~~ 2015.

Mätzler, C., ed.: Thermal Microwave Radiation: Applications for Remote Sensing, no. 52 in IET Electromagnetic Waves Series, IET, London, ISBN 978-0-86341-573-9 978-1-84919-002-2, https://doi.org/10.1049/PBEW052E, 2006.

Mätzler, C. and Wiesmann, A.: Documentation for MEMLS, Version 3, Microwave Emission Model of Layered Snowpacks, Tech. rep., Institute for Applied Physics, University of Bern, Bern, Switzerland, 2012.

Meier, W. and Notz, D.: A note on the accuracy and reliability of satellite-derived passive microwave estimates of sea-ice extent, Clic Arctic sea ice working group, Consensus document, CLIC International Project Office, 2010.

Meier, W. N. and Stewart, J. S.: Assessment of the Stability~~of Passive~~ of ~~MicrowaveBrightness~~ Passive Microwave Brightness Temperatures~~for NASA~~ for ~~TeamSea Ice Concentration~~ NASA Team Sea Ice Concentration Retrievals, Remote Sensing, 12, 2197, https://doi.org/10.3390/rs12142197, 2020.

Meier, W. N. and Stroeve, J.: Comparison of ~~sea-ice extent and ice-edge location estimates from passive microwave and enhanced-resolution scatterometer data~~Sea-Ice Extent and Ice-Edge Location Estimates from Passive Microwave and Enhanced-Resolution Scatterometer Data, Annals of Glaciology, 48, 65–70, https://doi.org/10.3189/172756408784700743, 2008.

Meier, W. N., Markus, T., Comiso, J., Ivanoff, A., and Miller, J.: Sea ~~ice algorithm theoretical basis document~~Ice Algorithm Theoretical Basis Document, Tech. Rep., 2017.

Meier, W. N., Fetterer, F., Windnagel, A. K., Stewart, J. S., and Stafford, T.: NOAA/NSIDC Climate Data Record of Passive Microwave Sea Ice Concentration, https://doi.org/10.7265/b18j-z797, g02202, Version 6. [Data Set]. Boulder, Colorado USA. National Snow and Ice Data Center, 2026.

Meissner, T. and Wentz, F.: An ~~updated analysis of the ocean surface wind direction signal in passive microwave brightness temperatures~~Updated Analysis of the Ocean Surface Wind Direction Signal in Passive Microwave Brightness Temperatures, IEEE Transactions on Geoscience and Remote Sensing, 40, 1230–1240, https://doi.org/10.1109/TGRS.2002.800231, 2002.

Meissner, T. and Wentz, F.: The ~~complex dielectric constant of pure and sea water from microwave satellite observations~~Complex Dielectric Constant of Pure and Sea Water from Microwave Satellite Observations, IEEE Transactions on Geoscience and Remote Sensing, 42, ~~1836 – 1849~~1836–1849, 2004.

Meshkov, A. I. and De Lucia, F. C.: Laboratory Measurements of Dry Air Atmospheric Absorption with a Millimeter Wave Cavity Ringdown Spectrometer, Journal of Quantitative Spectroscopy and Radiative Transfer, 108, 256–276, https://doi.org/10.1016/j.jqsrt.2007.04.001, 2007.

Monahan, E. and Lu, M.: Acoustically ~~relevant bubble assemblages and their dependence on meteorological parameters~~Relevant Bubble Assemblages and Their Dependence on Meteorological Parameters, IEEE Journal of Oceanic Engineering, 15, 340–349, https://doi.org/10.1109/48.103530, 1990.

Montpetit, B., Royer, A., Roy, A., Langlois, A., and Derksen, C.: Snow Microwave Emission Modeling of Ice Lenses Within a Snowpack Using the Microwave Emission Model for Layered Snowpacks, IEEE Transactions on Geoscience and Remote Sensing, 51, 4705–4717, https://doi.org/10.1109/TGRS.2013.2250509, 2013.

Morison, J. and McPhee, M.: ~~Ice–ocean~~ Ice–Ocean Interaction, in: Encyclopedia of ~~Ocean~~Ocean Sciences, pp. 1271–1281, Elsevier, ISBN 978-0-12-227430-5, https://doi.org/10.1006/rwos.2001.0003, 2001.

~~Mätzler, C., ed.: Thermal MicrowaveRadiation: Applicationsfor RemoteSensing, no. 52 in IETelectromagnetic waves series, IET, London, ISBN 978-0-86341-573-9 978-1-84919-002-2, , 2006.~~

Naoki, K., Ukita, J., Nishio, F., Nakayama, M., Comiso, J. C., and Gasiewski, A.: Thin Sea Ice Thickness as Inferred from Passive Microwave and in Situ Observations, Journal of Geophysical Research: Oceans, 113, 2007JC004 270, https://doi.org/10.1029/2007JC004270, 2008.

Nicolaus, M., Haas, C., and Willmes, S.: Evolution of ~~first-year and second-year snow properties on sea ice~~ First-year and Second-year Snow Properties on Sea Ice in the ~~Weddell~~Weddell Sea~~during spring-summer transition~~ during Spring-summer Transition, Journal of Geophysical Research: Atmospheres, 114, 2008JD011 227, https://doi.org/10.1029/2008JD011227, 2009.

Niederdrenk, A. L. and Notz, D.: Arctic Sea Ice in a 1.5°C Warmer World, Geophysical Research Letters, 45, 1963–1971, https://doi.org/10.1002/2017GL076159, 2018.

Nose, T., Waseda, T., Kodaira, T., and Inoue, J.: Satellite-Retrieved Sea Ice Concentration Uncertainty and Its Effect on Modelling Wave Evolution in Marginal Ice Zones, The Cryosphere, 14, 2029–2052, https://doi.org/10.5194/tc-14-2029-2020, 2020.

Notz, D. and Worster, M. G.: In Situ Measurements of the Evolution of Young Sea Ice, Journal of Geophysical Research: Oceans, 113, 2007JC004 333, https://doi.org/10.1029/2007JC004333, 2008.

Notz, D. and Worster, M. G.: Desalination ~~processes of sea ice revisited~~Processes of Sea Ice Revisited, Journal of Geophysical Research: Oceans, 114, 2008JC004 885, https://doi.org/10.1029/2008JC004885, 2009.

Oelke, C.: Atmospheric Signatures in Sea-Ice Concentration Estimates from Passive Microwaves: Modelled and Observed, International Journal of Remote Sensing, 18, 1113–1136, https://doi.org/10.1080/014311697218601, 1997.

Parkinson, C. L. and Cavalieri, D. J.: Arctic ~~sea ice variability and trends, 1979–2006~~Sea Ice Variability and Trends, 1979–2006, Journal of Geophysical Research: Oceans, 113, https://doi.org/10.1029/2007jc004558, ~~publisher: American Geophysical Union (AGU),~~ 2008.

Paul, F., Mielke, T., Schwarz, C., ~~Schröder~~Schröder, J., Rampai, T., Skatulla, S., Audh, R. R., Hepworth, E., Vichi, M., and Lupascu, D. C.: Frazil Ice in the ~~AntarcticMarginalIce~~ Antarctic Marginal Ice Zone, Journal of Marine Science and Engineering, 9, 647, https://doi.org/10.3390/jmse9060647, ~~publisher: MDPI AG,~~ 2021.

Petrich, C. and Eicken, H.: Overview of ~~sea ice growth and properties~~Sea Ice Growth and Properties, in: Sea Ice, edited by Thomas, D. N., pp. 1–41, Wiley, 1 edn., ISBN 978-1-118-77838-8 978-1-118-77837-1, https://doi.org/10.1002/9781118778371.ch1, 2017.

Picard, G., Royer, A., Arnaud, L., and Fily, M.: Influence of ~~meter-scale wind-formed features on the variability of the microwave brightness temperature~~ Meter-Scale Wind-Formed Features on the Variability of the Microwave Brightness Temperature around ~~Dome~~Dome C in Antarctica, The Cryosphere, 8, 1105–1119, https://doi.org/10.5194/tc-8-1105-2014, 2014.

Picard, G., Sandells, M., and ~~Löwe~~Löwe, H.: SMRT~~: an active–passive microwave radiative transfer model for snow with multiple microstructure and scattering formulations~~ : An Active–Passive Microwave Radiative Transfer Model for Snow with Multiple Microstructure and Scattering Formulations (v1.0), Geoscientific Model Development, 11, 2763–2788, https://doi.org/10.5194/gmd-11-2763-2018, 2018.

Picard, G., ~~Löwe~~Löwe, H., Domine, F., Arnaud, L., Larue, F., Favier, V., Le Meur, E., Lefebvre, E., Savarino, J., and Royer, A.: The ~~MicrowaveSnowGrain~~ Microwave Snow Grain Size~~: A~~: ~~New~~A New Concept to ~~PredictSatelliteObservations~~ Predict Satellite Observations Over Snow~~Over -Snow-~~Covered Regions, AGU Advances, 3, e2021AV000 630, https://doi.org/10.1029/2021AV000630, ~~2022.~~ 2022a.

Picard, G., Löwe, H., and Mätzler, C.: Brief Communication: A Continuous Formulation of Microwave Scattering from Fresh Snow to Bubbly Ice from First Principles, The Cryosphere, 16, 3861–3866, https://doi.org/10.5194/tc-16-3861-2022, 2022b.

Polder, D. and Van Santeen, J.: The ~~effective permeability of mixtures of solids~~Effective Permeability of Mixtures of Solids, Physica, 12, 257–271, https://doi.org/10.1016/S0031-8914(46)80066-1, 1946.

Purich, A. and Doddridge, E. W.: Record ~~low~~ Low Antarctic~~sea ice coverage indicates a new sea ice state~~ Sea Ice Coverage Indicates a New Sea Ice State, Communications Earth & Environment, 4, 314, https://doi.org/10.1038/s43247-023-00961-9, 2023.

Soriot, C., Picard, G., Prigent, C., Frappart, F., and Domine, F.: ~~Year-round sea ice and snow characterization from combined passive and active microwave observations and radiative transfer modeling~~Year-Round Sea Ice and Snow Characterization from Combined Passive and Active Microwave Observations and Radiative Transfer Modeling, Remote Sensing of Environment, 278, 113 061, https://doi.org/10.1016/j.rse.2022.113061, 2022.

Spreen, G., Kaleschke, L., and Heygster, G.: Sea Ice Remote Sensing Using AMSR-E 89-GHz Channels, Journal of Geophysical Research: Oceans, 113, 2005JC003 384, https://doi.org/10.1029/2005JC003384, 2008.

Steffen, K. and Schweiger, A.: NASA~~team algorithm for sea ice concentration retrieval from Defense~~ Team Algorithm for Sea Ice Concentration Retrieval from ~~MeteorologicalSatellite~~ Defense Meteorological Satellite Program~~special sensor microwave imager~~ Special Sensor Microwave Imager: Comparison with Landsat~~satellite imagery~~ Satellite Imagery, Journal of Geophysical Research: Oceans, 96, 21 971–21 987, https://doi.org/10.1029/91JC02334, 1991.

Strong, C. and Rigor, I. G.: Arctic Marginal Ice Zone Trending Wider in Summer and Narrower in Winter, Geophysical Research Letters, 40, 4864–4868, https://doi.org/10.1002/grl.50928, 2013.

Swift, C. T., Fedor, L. S., and Ramseier, R. O.: An ~~algorithm to measure sea ice concentration with microwave radiometers~~Algorithm to Measure Sea Ice Concentration with Microwave Radiometers, Journal of Geophysical Research: Oceans, 90, 1087–1099, https://doi.org/10.1029/jc090ic01p01087, ~~publisher: American Geophysical Union (AGU),~~ 1985.

Tonboe, R. T.: The Simulated Sea Ice Thermal Microwave Emission at Window and Sounding Frequencies, Tellus A, 62, 333–344, https://doi.org/10.1111/j.1600-0870.2010.00434.x, 2010.

Tonboe, R. T., Dybkjær, G., and Høyer, J. L.: Simulations of the Snow Covered Sea Ice Surface Temperature and Microwave Effective Temperature, Tellus A: Dynamic Meteorology and Oceanography, 63, 1028, https://doi.org/10.1111/j.1600-0870.2011.00530.x, 2011.

Tonboe, R. T., Eastwood, S., Lavergne, T., Sørensen, A. M., Rathmann, N., Dybkjær, G., Pedersen, L. T., Høyer, J. L., and Kern, S.: The EUMETSAT Sea Ice Concentration Climate Data Record, The Cryosphere, 10, 2275–2290, https://doi.org/10.5194/tc-10-2275-2016, 2016.

Tonboe, R. T., Nandan, V., Makynen, M., Pedersen, L. T., Kern, S., Lavergne, T., Oelund, J., Dybkjaer, G., Saldo, R., and Huntemann, M.: Simulated Geophysical Noise in Sea Ice Concentration Estimates of Open Water and Snow-Covered Sea Ice, IEEE Journal of Selected Topics in Applied Earth Observations and Remote Sensing, 15, 1309–1326, https://doi.org/10.1109/JSTARS.2021.3134021, 2022.

Tonboe, R. T., Nandan, V., Huntemann, M., Stroeve, J., Scharien, R., Yackel, J., Kaleschke, L., Shi, H., and Casal, T.: Estimation of sea ice air-bubble and brine pocket distribution for scattering and emission model parametrization, EGUsphere [preprint], https://doi.org/10.5194/egusphere-2026-1440, 2026.

Torquato, S. and Kim, J.: Nonlocal Effective Electromagnetic Wave Characteristics of Composite Media: Beyond the Quasistatic Regime, Physical Review X, 11, 021 002, https://doi.org/10.1103/PhysRevX.11.021002, 2021.

Toyota, T., Massom, R., Tateyama, K., Tamura, T., and Fraser, A.: Properties of ~~snow overlying the sea ice~~ Snow Overlying the Sea Ice off ~~East~~East Antarctica~~in late winter~~ in Late Winter, 2007, Deep Sea Research Part II: Topical Studies in Oceanography, 58, 1137–1148, https://doi.org/10.1016/j.dsr2.2010.12.002, 2011.

Tsang, L., Kong, J. A., and Shin, R. T.: Theory of ~~microwave remote sensing, Wiley series in remote sensing~~Microwave Remote Sensing, Wiley Series in Remote Sensing, Wiley, New York, ISBN 978-0-471-88860-4, 1985.

Vichi, M.: An ~~indicator of sea ice variability~~ Indicator of Sea Ice Variability for the Antarctic~~marginal ice zone~~ Marginal Ice Zone, The Cryosphere, 16, 4087–4106, https://doi.org/10.5194/tc-16-4087-2022, ~~number: 10,~~ 2022.

Wang, Z., Fraser, A. D., Reid, P., O~~'~~'Farrell, S., and Coleman, R.: Antarctic ~~sea ice surface temperature bias in atmospheric reanalyses induced by the combined effects of sea ice and clouds~~Sea Ice Surface Temperature Bias in Atmospheric Reanalyses Induced by the Combined Effects of Sea Ice and Clouds, Communications Earth & Environment, 5, 552, https://doi.org/10.1038/s43247-024-01692-1, 2024.

Weeks, W. and Lee, O.: The Salinity Distribution in Young Sea-Ice, ARCTIC, 15, 92–108, https://doi.org/10.14430/arctic3562, 1962.

Willmes, S., Nicolaus, M., and Haas, C.: The ~~microwave emissivity variability of snow covered first-year sea ice from late winter to early summer: a model study~~Microwave Emissivity Variability of Snow Covered First-Year Sea Ice from Late Winter to Early Summer: A Model Study, The Cryosphere, 8, 891–904, https://doi.org/10.5194/tc-8-891-2014, 2014.

Worby, A.: Studies of the ~~Antarcticsea ice edge and ice extent from satellite and ship observations, Remote Sensing of Environment, 92, 98–111, , 2004.~~

~~Worby, A.: Studies of the~~ Antarctic~~sea ice edge and ice extent from satellite and ship observations~~ Sea Ice Edge and Ice Extent from Satellite and Ship Observations, Remote Sensing of Environment, 92, 98–111, https://doi.org/10.1016/j.rse.2004.05.007, ~~2004.~~ 2004.

Yin, X., Boutin, J., Dinnat, E., Song, Q., and Martin, A.: Roughness and ~~foam signature~~ Foam Signature on ~~SMOS-MIRAS~~SMOS-MIRAS~~brightness temperatures~~ Brightness Temperatures: A~~semi-theoretical approach~~ Semi-Theoretical Approach, Remote Sensing of Environment, 180, 221–233, https://doi.org/10.1016/j.rse.2016.02.005, 2016.